ELSEVIER

Rigorous dynamic model of a direct methanol fuel cell based on Maxwell–Stefan mass transport equations and a Flory–Huggins activity model: Formulation and experimental validation

Thorsten Schultz[a], Kai Sundmacher[a,b],*

[a] *Max Planck Institute for Dynamics of Complex Technical Systems, Sandtorstrasse 1, 39106 Magdeburg, Germany*
[b] *Otto-von-Guericke University Magdeburg, Process Systems Engineering, Universitätsplatz 2, 39106 Magdeburg, Germany*

Abstract

A one-dimensional rigorous process model of a single-cell direct methanol fuel cell (DMFC) is presented. Multi-component mass transport in the diffusion layers and the polymer electrolyte membrane (PEM) is described using the generalised Maxwell–Stefan (MS) equation for porous structures. In the PEM, also local swelling behaviour and non-idealities are accounted for by a Flory–Huggins model for the activities of the mobile species inside the pores of the PEM. Phase equilibria between the pore liquid inside the PEM and those inside the pores of both catalyst layer are formulated based on literature data and activity models. Although two-phase behaviour in both diffusion layers is neglected, the model shows good agreement to own experimental data over a wide range of operating conditions, with respect to methanol and water crossover fluxes as well as to current–voltage characteristics. Only for very low current densities and in the limiting current regime significant deviations between model and experiments are found.
© 2005 Elsevier B.V. All rights reserved.

Keywords: Direct methanol fuel cell; Model; Multi-component mass transport; Maxwell–Stefan; Flory–Huggins

1. Introduction

Since first direct methanol fuel cell (DMFC) systems are commercially available for special outdoor and professional applications (e.g. from SmartFuelCell GmbH, Germany), the prospects of this type of fuel cell are gaining an even higher interest in the consumer electronics industry. The first commercial systems prove the practical value and applicability of the DMFC, but also the challenges still ahead. The fuel efficiencies and the power densities are still very low, and a reliable dynamic operation without a significant buffer for electrical energy (like e.g. a battery or a supercapacitor) has not yet been reported.

The necessary improvements in DMFC performance and operation do not only place the demand for better materials, i.e. better catalysts and a polymer electrolyte membrane (PEM) less or even impermeable for methanol and water, but also for sophisticated controller designs. Only the lat-

Nomenclature

a	activity (–)
$a_{H_2O}^*$	water vapour activity (–)
A^S	cell cross-sectional area (m^2)
A_i	parameter in empirical correlations (–)
B	transport matrix
B_0	permeability coefficient (mm^2)
B_i	parameter in empirical correlations (–)
c	molar concentration in fluid-phase (mol m^{-3})
$\tilde{c}$	molar pseudo-concentration w.r.t. total volume (in porous structures only) (mol m^{-3})
C_i	parameter in empirical correlations (–)
C_p	mass-based heat capacity at constant pressure (J kg^{-1}K^{-1})
$\bar{C}_p$	molar heat capacity at constant pressure (J mol^{-1}K^{-1})
$\Delta_R \bar{C}_p$	molar heat capacity change of reaction at constant pressure (J mol^{-1}K^{-1})
d	thickness, diameter (m)
D	diffusion coefficient (mm^2 s^{-1})
$Đ$	Maxwell–Stefan binary diffusion coefficient (m^2 s^{-1})
D_i	parameter in empirical correlations (–)
e	enthalpy flux density (J m^{-2} s^{-1})
E^A	activation energy (J mol^{-1})
E_i	parameter in empirical correlations (–)
F	Faraday's constant, $F = 96485\,\text{A s mol}^{-1}$(A s mol^{-1})
$\Delta_F G$	Gibbs energy of formation (from the elements) (J mol^{-1})
$\Delta_R G$	Gibbs energy of reaction (J mol^{-1})
h	specific enthalpy (J mol^{-1})
$\Delta_F H$	enthalpy of formation (from the elements) (J mol^{-1})
$\Delta_R H$	reaction enthalpy (J mol^{-1})
i	current density (A m^{-2})
j	individual molar flux density (mol m^{-2} s^{-1})
k	index for control volumes (discretised model) (–)
L_i	friction terms (s m^{-2})
m	mass flux density (kg m^{-2} s^{-1})
M	mass (kg)
$\bar{M}$	molar mass (kg mol^{-1})
n	overall molar flux density (mol m^{-2} s^{-1})
N	number of moles (mol)
$\hat{N}$	mole density (loading, used only in polymer material) (mol m^{-2})
$N_{M,cu}$	number of chain units between two polymer cross-links (–)
p	pressure (Pa)
p_{sat}	saturation pressure (Pa)
P	parachor (cm^3 g$^{0.25}$ s$^{-0.5}$)

q	heat flux density (due to thermal conduction) (J m^{-2} s^{-1})
Q	charge (C = As)
$\hat{Q}$	charge density w.r.t. cross-sectional area (C m^{-2})
$\tilde{Q}$	volumetric charge density w.r.t. total volume (C m^{-3})
r	reaction rate (mol m^{-3} s^{-1})
R	ideal gas constant, $R = 8.314\,\text{J mol}^{-1}\,\text{K}^{-1}$ (J mol^{-1} K^{-1})
t	time (s)
T	temperature (K)
U	voltage (V)
v	velocity (m s^{-1})
V	volume (m^3)
$\bar{V}$	molar volume (m^3 mol^{-1})
$(\sum \bar{V}^*)$	atomic diffusion volumes (cm^3 mol^{-1})
w	mass fraction (–)
x	mole fraction in liquid-phase (–)
y	mole fraction in gas-phase (–)
z	cell coordinate perpendicular to cell plane (m)
z^*	number of transferred electrons/single charges (–)

Greek symbols

α	heat transfer coefficient (W m^{-2} K^{-1})
α_a, α_c	charge transfer coefficients (anodic, cathodic) (–)
α_{Vignes}	thermodynamic factor (Vignes method) (–)
α'	viscous selectivity factor (–)
κ	ratio of specific heat capacities, chapter A.8 (–)
Γ	volumetric charge production (C m^{-3} s^{-1})
ε	volume fraction (pore volume fraction = porosity) (–)
η	overpotential (V)
η^{vis}	dynamic viscosity (Pa s)
λ	thermal conductivity coefficient (W m^{-1} K^{-1})
Λ	relative water content in membrane (–)
μ	chemical potential (J mol^{-1})
μ^{vis}	kinematic viscosity (mm^2 s^{-1})
ν	stoichiometric coefficient (–)
ρ	mass density (kg m^{-3})
τ	tortuosity factor (–)
ϕ	electrical potential (V)
χ	non-ideality coefficient in Flory–Huggins activity model (–)

Superscripts

A	anode compartment (supply channel structure)
AC	anode catalyst layer
ACP	polymer phase within (AC)
AD	anode diffusion layer
AF	anode feed

C	cathode compartment (supply channel structure)
CC	cathode catalyst layer
CCP	polymer phase within (CC)
CD	cathode diffusion layer
CF	cathode feed
eff	effective
M	membrane (PEM)
vis	viscosity
θ	at standard conditions: $T^\theta = 298\,\mathrm{K}$, $p^\theta = 10^5\,\mathrm{Pa}$

Subscripts

a	anode
air	air
BET	BET surface
c	cathode
carbon	carbon material
cat	catalyst
cat.layer	catalyst layer
cell	cell
cross	crossover
cu	polymer chain unit
CH_3OH	methanol
CO_2	carbon dioxide
dry	dry
eff	effective
eq	equilibrium
F	feed
gas	gas
(g)	in gas state
graphite	graphite material
H^+	proton
H_2O	water
i	counting index
j	counting index
Joule	Joule heating
liquid	liquid
(l)	in liquid state
M	solid matrix in porous materials
N_2	nitrogen
O_2	oxygen
p	at constant pressure
pores	in pore(s)
P	polymer
PTFE	PTFE (polytetrafluorethylene, TEFLON™)
PTFE-treated Toray	TORAY™ carbon paper, treated with PTFE
sat	saturated
sound	sound
untreated Toray	TORAY™ carbon paper, as supplied by manufacturer
wet	wet

ter could e.g. enable reliable dynamic operation with a minimised buffer for electrical energy, as long as no significantly improved materials for the DMFC are available. Also, clever control strategies could possibly enhance the power density and thus the fuel efficiency [1].

Both tasks, material development as well as controller design, can only be effectively addressed if realistic mathematical process models are available. In the field of fuel cells in general, a number of publications address this topic, but mainly in the area of hydrogen-fed polymer electrolyte membrane fuel cells (PEMFC). For the liquid-fed DMFC (l-DMFC) only a small number of mathematical models has been published. Table 1 shows a systematic comparison of recent publications (since 1997) with respect to the key features of mathematical fuel cell models. In the first column of the table the respective reference numbers are given.

The second column of Table 1 shows whether the presented models are dynamic (dyn.) or steady-state (s.s.). Here it becomes evident, that except for publications from our group [1,2] (also including this paper), all published models are steady-state, i.e. they are used to predict steady-state current voltage characteristics and concentration profiles.

The next block of seven columns presents the dimensionality of the models in the seven functional layers of a DMFC (A = anode compartment/flow channels, AD = anode diffusion layer, AC = anode catalyst layer, M = membrane/PEM, CC = cathode catalyst layer, CD = cathode diffusion layer, C = cathode compartment/flow channels). A blank indicates that this part of the DMFC is not included in the model, a zero means that this element is described by a lumped parameter model (usually as an ideally mixed-phase) and a "1" means that this element is modeled one-dimensional. In case of the flow channels (A,C) this usually means along the channel, while for the inner layers of the DMFC this means perpendicular to the cell plane. One can see from Table 1, that with respect to the spatial model structure the different models vary significantly, depending on the focus of the respective work. A number of models does not account for the cathode side gas transport to the cathode catalyst layer, assuming this contribution not to be dominating for the respective operating conditions [1,3–7,2]. The model to be presented in this work covers all structural layers of the DMFC.

In the next two columns of Table 1, the type of the applied electrode kinetic expressions is presented. In most l-DMFC models simple Tafel type rate expressions are applied, only few papers use Butler–Volmer (BV) type expressions [1,5,2] which are also able to predict open-circuit overpotentials. Some models even use more realistic, complex multi-step reaction kinetics for the electrochemical methanol oxidation [1,2,6,8–11].

The next two columns of Table 1 compare the description of the phase situation in the anode and cathode pore structures. It is well known that in the l-DMFC under a variety of operating conditions, on the anode as well as on the cathode side a liquid (l) and a gas (g) phase can coexist. On the anode side this is due to the production of carbon diox-

Table 1
Comparison of l-DMFC models published since 1997

Reference	dyn./s.s.	Dimensionality							Phase situation		Electrode kinetics		Mass transport models			Membrane swelling	Energy balance
		(A)	(AD)	(AC)	(M)	(CC)	(CD)	(C)	Anode	Cathode	Anode	Cathode	Anode	Membrane	Cathode		
1, 2	dyn.	0	0	0	1	0	–	–	l	g	Complex	BV	eff.F	NP+S	–	–	Isothermal
3	s.s.	0	0	1	0	1	–	–	l	g	Tafel	Tafel	–	NP+dc	–	–	Isothermal
4	s.s.	0	1	0	0	0	–	–	g+l	g	Tafel	Tafel	eff.F	NP+dc	–	–	Isothermal
5	s.s.	0	0	0	0	0	–	–	g+l	g	BV	BV	NP+S	NP+S	–	–	Isothermal
6	s.s.	0	1	1	–	–	–	–	l	–	Complex	–	NP	NP+dc	–	–	Isothermal
7	s.s.	0	1	1	0	–	–	–	l	–	Tafel	–	NP	NP+dc	–	–	Isothermal
8	s.s.	0	1	1	1	1	1	0	g+l	g+l	Complex	Tafel	NP(l),MS(g)	NP+irrev.TD	SD(l),MS(g)	Empiric	Isothermal
9 + 10 + 11	s.s.	–	1	1	1	1	1	–	g+l	g	Complex	Tafel	NP(l),MS(g)	MS	MS	TD model	Isothermal
12	s.s.	0	0	1	1	0	0	0	g+l	g+l	Tafel	Tafel	NP	NP+S	NP(l),MS(g)	–	Isothermal
13	s.s.	0	0	0	0	0	0	0	g+l	g+l	Tafel	Tafel	eff.F	–	eff.F	–	Isothermal
14	s.s.	1	1	1	1	1	1	1	l	g	Tafel	Tafel	F	NP+dc	F	–	Isothermal
This paper	dyn.	0	1	0	1	1	1	0	l	g	BV	BV	MS	MS	MS	TD model	Full balance

BV: Butler–Volmer; dc: drag coefficient; dyn.: dynamic; eff.: effective; F: Fick' g: gas; irrev.: irreversible; l: liquid; MS: Maxwell–Stefan dynamic; NP: Nernst–Planck (=Fick +convection); S: Schlögl; SD: surface diffusion; s.s.: steady-state; TD: Thermodynamics.

ide in the anode catalyst layer and the low solubility of this gas in liquid water methanol solutions, especially at elevated temperatures. Therefore, carbon dioxide bubbles are formed. Whether this takes place within the porous catalyst and diffusion layer structures or only within the flow channels is still under discussion, but a variety of models assumes two-phase flow inside the anode pore structure [4,5,8–13]. Inside the cathode pore structure, product water may condense and block the way for fresh oxygen. This phenomenon is usually referred to as cathode flooding. Also here it is not fully clear, whether such condensation can occur within the (usually hydrophobic) cathode diffusion layer, or only on the surface of the diffusion layer inside the flow channels. Nonetheless, such two-phase behaviour on the cathode side is covered by a few models [8,12,13]. All other models assume pure liquid-phase on the anode side, and pure gas-phase on the cathode side of the l-DMFC.

A very important feature of each l-DMFC model are the chosen mass transport descriptions in the anode and cathode structures and inside the polymer electrolyte membrane. Several types of mass transport models are applied. Simple Fick diffusion models (F) and effective Fick models (eff.F) (using – usually experimentally determined – effective transport coefficients instead of Fick diffusivities) do not account for convective flow contributions [1,2,4,13,14]. Therefore, many models feature Nernst–Planck (NP) mass transport expressions, which combine Fick diffusion with a superposed convective flow [1–12,14]. The latter is usually calculated from Darcy's law using different formulations of the hydraulic permeability coefficient. Instead of Darcy's law, also some models use Schlögl's formulation (S) for the convective flow [1,2,5,12]. This also accounts for electro-osmotic flow and can thus also be used for mass transport inside the PEM. An alternative, very simple way of incorporating electro-osmotic flow in the membrane mass transport is applying so-called drag coefficient models (dc) which assume a proportionality of the convective water and methanol flow to the proton flow [3,4,6,7,14]. The last popular type of mass transport description is the Maxwell–Stefan formulation for multi-component mixtures. But it is often only applied to gas-phase transport [8,12]. Only one model so far (except for this paper) uses this formulation also for (liquid-phase) mass transport inside the PEM [9–11]. Rarely used for liquid flow are surface diffusion models (50), or models derived from irreversible thermodynamics (irrev.TD) [8]. All mass transport models applying effective transport coefficients and drag coefficients (F, eff.F, NP, S) usually only yield good approximations to experimental data for a very limited range of operating conditions, unless the coefficients are formulated as functions of the operating conditions (most important is the temperature dependence of all mass transport parameters).

The second last column of Table 1 presents, whether the l-DMFC models account for varying water contents inside the PEM, i.e. the swelling behaviour of these materials. Most models assume a fully hydrated PEM, as on the anode side liquid water as excess component is present. Only few mod-

els skip this assumption. In one case [8] the water uptake of the PEM is described by an empiric correlation (developed from experimental data), in another [9–11] a thorough thermodynamic (TD) model is formulated based on change of free Gibbs energy inside the PEM according to local water content. Also in this paper, a thermodynamic model will be presented to account for local PEM swelling.

Finally, the last column of Table 1 compares the published l-DMFC models with respect to inclusion of energy balances. Obviously all published models assume an isothermal cell operation, therefore no energy balances are formulated. The model to be presented in this paper is the first comprising a full energy balance.

Summing up, in this work a one-dimensional model of a l-DMFC will be presented, which is different from so-far published models in several respects:

- The model is dynamic, allowing also to predict dynamic operation (not presented in this paper).
- The model consequently uses a Maxwell–Stefan model for all types of mass transport in all functional layers. This enables to predict mass transport correctly for a vast range of operating conditions (especially cell temperatures between ambient and 90 °C) with one single set of mass transport parameters.
- Membrane water uptake and (local) swelling behaviour are accounted for by applying a Flory–Huggins activity model.
- Heat conduction and local heat production are fully accounted for by a complete energy balancing.

The mean simplifications of the model are:

- Assumption of pure liquid-phase in the anode structures and pure gas phase in the cathode structures.
- No spatial discretisation of catalyst layers.
- Application of Butler–Volmer type rate expressions for both electrode reactions.

To evaluate the model, experiments were performed in which methanol and water crossover fluxes through the PEM were measured (together with the cell voltage) under a variety of operating conditions (anode feed temperatures from 30 to 90 °C, full range of cell current densities).

In this paper, the focus will be on describing the structure of the model and presenting the results. More details, especially with respect to the mass transport and the Flory–Huggins activity model of the PEM, phase equilibria between PEM and the catalyst layers, the derivation of all model parameters, as well as a number of additional experimental results can be found in [15].

2. Experiments

To be able to measure methanol and water crossover fluxes in a DMFC, a fully automated miniplant was constructed and an own DMFC design was developed in order to be able to

influence all materials and structures within the DMFC. In the following, the miniplant and the in-house DMFC design will be shortly presented.

2.1. Applied in-house DMFC design

The experiments were carried out using a single cell DMFC fed with air and liquid–methanol–water solutions. A detailed description of the DMFC design can be found in [15].

The identical anode and cathode monopolar plates are made from graphite material (thickness 7 mm, material code FU4369) supplied by Schunk Kohlenstofftechnik (Germany). The necessary flowbed structures for the reactant distribution over the MEA surface are millcut into the plates (Fig. 1). They consist of parallel channels of 2 mm width and 2 mm depth, with 1 mm wide ribs between them. A distributor (Fig. 1, top) and collector channel (Fig. 1, bottom) connect the parallel channels to the inlet and outlet ports, respectively. The media (air and methanol–water solution) are supplied in one corner of the rectangular flowbed and leave at the opposite corner (flow direction indicated in Fig. 1). The flowbed itself has the outer dimensions 65 mm × 40 mm, identical to the catalyst layer on the MEAs, which leads to an active area of $A^S = 26$ cm^2.

As diffusion layers PTFE-coated TORAY carbon paper (TGP-H-060) is used, with a PTFE loading between 20 and 25 mass% with respect to the uncoated material.

Finally, the membrane electrode assemblies (MEA) are prepared from NAFION™ N-105 membrane foil, onto which the catalyst layers are applied using an airbrush technique refined by ZSW Ulm (Germany) [16]. The anode catalyst layer features a catalyst loading of 5 mg cm^{-2} (unsupported) platinum ruthenium black (Alfa Aesar Johnson Matthey HiSPEC™ 6000) and a NAFION™ content of 15 mass% relative to the metal loading (i.e. 0.75 mg cm^{-2}). The cathode catalyst layer has the same metal loading, but as catalyst
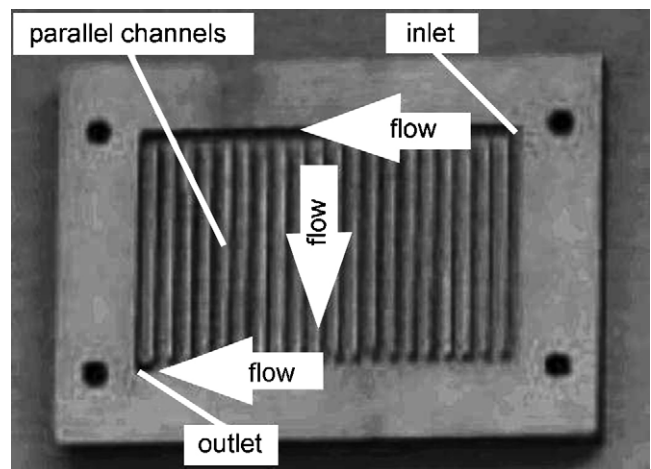

Fig. 1. Photo of monopolar plate showing inlet, outlet and flow direction in flowbed structure.

(unsupported) platinum black is used (Alfa Aesar Johnson Matthey HiSPEC™ 1000) and the NAFION™ content is 10 mass% relative to the metal loading (i.e. 0.5 mg cm^{-2}).

The DMFC is completed by gold-plated copper plates as current collectors and stainless steel plates for bracing the whole sandwich structure. A torque of 5 Nm is exerted on the screws, which hold together the steel back plates. After assembly, each DMFC is conditioned and evaluated by operation with pure humidified hydrogen and air for three times 8 h, before it is operated on methanol solutions.

2.2. Experimental setup

For automated testing of DMFCs, a miniplant was designed using the process control system PC-S7/WinCC by Siemens. It enables automatic testing procedures, with a special focus on dynamic operation. Fig. 2 shows a simplified flowsheet of the miniplant. All details can be found in [15].

The DMFC cathode is supplied with dry air (dew point ~3 °C) at flow rates between 0.4 and 5.0 scbm h^{-1} (mass flow controller F101, type Mass6020 by Bürkert AG, Germany) at cathode outlet pressures of ambient up to 5 bars absolute (1.5×10^5 Pa). The air is pre-heated in a plate heat exchanger (W101), air temperatures and pressures are measured at the cathode inlet and outlet. At the cathode outlet,

also the relative humidity of the air is measured (Q202, type HygroClip IE by rotronic AG, Switzerland). Finally the cathode exhaust air enters a condensor, where it is dried to reach a dew point below 10 °C (condensate is collected). The dry air is sent into a fume hood, while its oxygen and carbon dioxide contents are measured. The oxygen sensor (Q204) is a paramagnetic sensor (PAROX 1000 H by MBE AG, Switzerland), while carbon dioxide is measured using an FT-IR-sensor (Q203, type OEM-NDIR EGC-5% by Pewatron AG, Switzerland).

On the DMFC anode side, a liquid recycle loop is installed. It consists of two alternative cycles, one for methanol–water solution and one for pure water. The purpose of this is to enable a stepped or pulsed periodic operation of the DMFC, where the anode feed is changed stepwise between methanol–water solution and pure water automatically. Both branches of the anode cycle feature vessels for pressure equilibration and carbon dioxide removal (B1 and B2), gear pumps (P401 and P402) and heat exchangers (W403 and W406). Flow rates between 0.3 and 5 dm^3 min^{-1} can be achieved. Automatic valves (V403/V404 and V408/V409) enable a flexible and practically immediate change between methanol–water solution and pure water anode feed without causing significant disturbances in liquid flow rate and pressure. The flow rate is measured by a Coriolis-type sensor (F401, type MASS
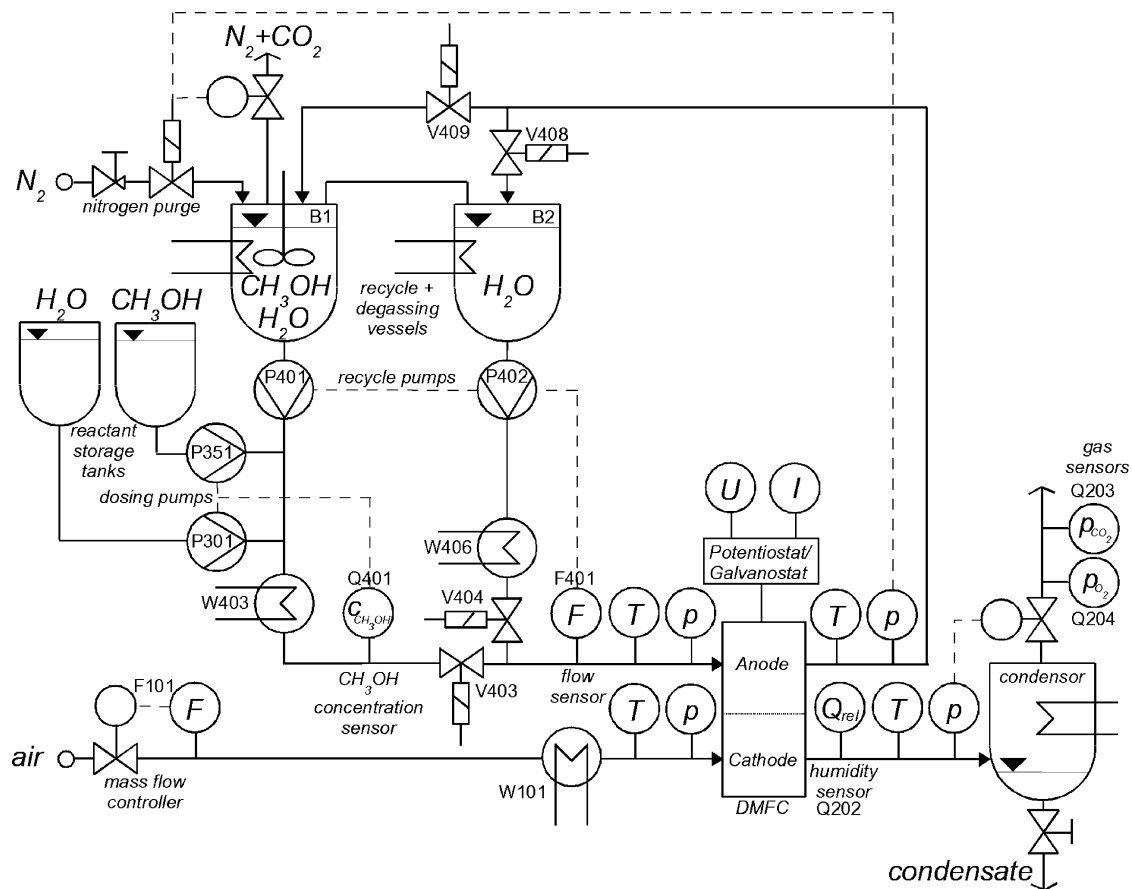

Fig. 2. Flow sheet (simplified) of DMFC miniplant with major components and sensors.

2100 DI6 by Danfoss, Denmark). Like on the cathode side, the medium temperature and pressure are measured at the cell inlet and outlet. The methanol concentration of the anode inlet medium is measured online using an ultrasound sensor (Q401, type LiquiSonic30 by SensoTech GmbH, Germany), based on the influence of the methanol concentration on the speed of sound in methanol–water solutions. This sensor is used in a methanol concentration controller, which as actuators uses two dosing pumps for pure methanol (P351) and pure water (P301) (mzr-2905 by HNP Mikrosysteme, Germany). Methanol concentrations between 0 and 1.5 mol dm^{-3} can be detected and controlled. The flow rates of the dosing pumps can be controlled in the range from 0.2 up to 18 cm^3 min^{-1}. To adjust the anode pressure and also to strip off carbon dioxide, the recycle vessels are equipped with a nitrogen purge/blanket. The anode pressure can be controlled in the range between ambient and 5 bars absolute (1.5 × 10^5 Pa). The liquid inlet temperature (which is also the DMFC temperature due to the applied high flow rates) can be controlled in the range between −20 and +90 °C (253, . . . , 363 K).

The DMFC is electrically connected to a potentiostat (HP60-50 by Wenking GmbH, Germany), which enables operation of fuel cells from below 1 W up to 1 kW at a maximum current of 50 A. Galvanostatic as well as potentiostatic operation is possible, with the possibility to automatically run user-defined load scenarios.

The array of sensors around the DMFC, i.e. potentiostat, flow rates, inlet and outlet concentrations of key components (oxygen, methanol, water, carbon dioxide) enables full online material balancing of these components. Assuming full and immediate oxidation of crossover methanol on the cathode catalyst, from the sensor information also the methanol and water crossover fluxes from anode to cathode (i.e. through the PEM) can be calculated (for details see [15]).

2.3. Performed experiments

The online balancing function of the miniplant allows to measure the steady-state methanol and water crossover fluxes through the PEM of the DMFC. These crossover fluxes (together with the current–voltage characteristics) were measured for a broad range of cell temperatures (30–90 °C) as functions of the cell current density. The experimental results are presented in chapter 4 (model validation) in comparison to simulation data. All operating conditions are given there.

3. Model formulation

In this chapter, a dynamic model of a single cell DMFC will be presented. This model represents the cross-sectional structure of the DMFC, which is depicted in Fig. 3. The model is one-dimensional, perpendicular to the cross-sectional area of the cell. All state variables are assumed to be constant in the other two space coordinates. As can be seen in Fig. 3, on this level of decomposition the cell consists of seven sequentially connected phases: anode and cathode compartments (i.e. the flowbeds), both diffusion and catalyst layers and the PEM in the middle.

3.1. Basic model assumptions

The basic model assumptions, which apply to all elements, are:

- all gas phases obey the ideal gas law,
- all inert gases (components of air, like nitrogen, argon etc.) are merged to "nitrogen",
- in liquid phases nonideal mixing behaviour is not accounted for, variations of activity coefficients are
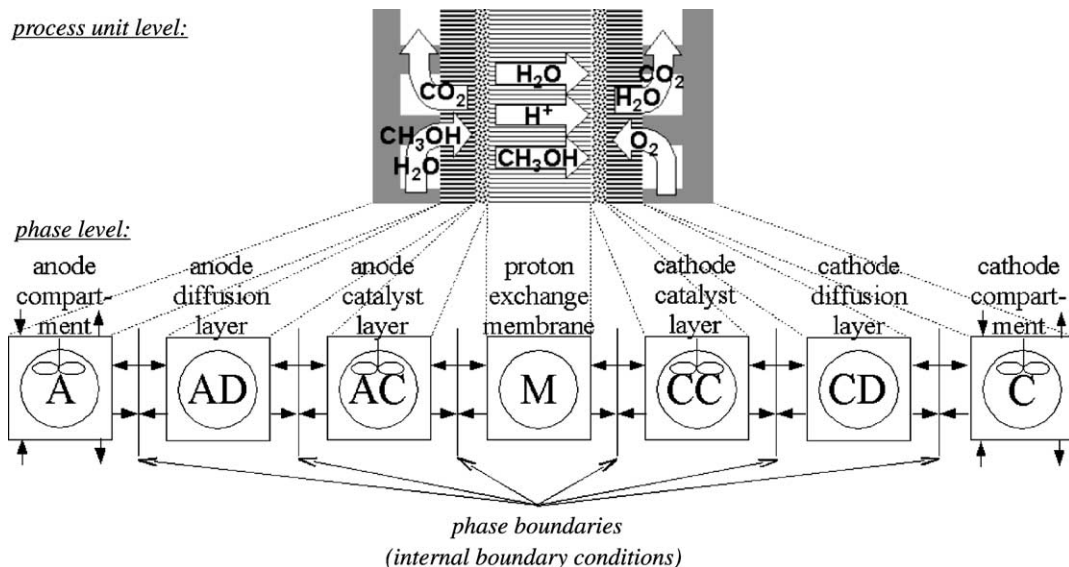

Fig. 3. Schematic of DMFC layers, component mass fluxes and model structure.

neglected due to the strong dilution of methanol in water (this assumption is not valid in the PEM),

- in each element, only the existence of one thermodynamic phase is assumed, i.e. on the anode side formation of carbon dioxide bubbles is neglected, on the cathode side the formation of a liquid-phase due to condensation (so-called cathode flooding),
- all charge balances are quasi-stationary,
- electroneutrality is assumed in the PEM,
- and finally, ohmic losses other than in the PEM are neglected.

To assume ideal gas behaviour seems justified, as the maximum system pressures do not exceed 5 bars (5×10^5 Pa) and the temperature range does not exceed $10, \ldots, 90\,°C$ ($283, \ldots, 363$ K). Also all components (methanol, water, oxygen, carbon dioxide and nitrogen) have a low molecular weight.

The assumption of solely single-phase behaviour is the major simplification of the model. Under a variety of practical operating conditions it has been observed, that liquid water forms in the cathode compartment and gas bubbles of carbon dioxide form in the anode compartment. The question which phase situation is present within the porous diffusion and catalyst layers, though, has not yet been answered satisfactorily.

The final assumption that no ohmic drops are accounted for other than that in the PEM is based on the fact that all electron conducting parts of the DMFC (bipolar plates, diffusion layers, catalyst layers) are made from very good electron conducting materials (graphite, noble metals), and that especially the diffusion and catalyst layers are very thin, while having a large contact area.

3.2. Mass transport and balancing

For the description of mass transport in porous structures, the generalised Maxwell–Stefan approach is used, in the formulation proposed by Krishna and Wesselingh [17,18]. It is based on a mechanical equilibrium between driving forces acting on a species j and friction forces between this species and all other species i around it:

$$-\frac{c_j}{RT}\nabla_{T,p}\mu_j - \frac{c_j}{RT}\bar{V}_j\nabla p - \frac{\alpha'_j}{Ð_{jM}}c_j\frac{B_0}{\eta^{vis}}\nabla p - c_j z_j^* \frac{F}{RT}\nabla\phi$$
$$= \sum_{i \neq j}\frac{x_i n_j - x_j n_i}{Ð_{ij}^{eff}} + \frac{n_j}{Ð_{jM}^{eff}} \tag{1}$$

On the left hand side of Eq. (1) are four terms describing the driving forces. Term one and two describe diffusive driving forces resulting from gradients in the chemical potentials μ_j (J mol^{-1}) (first term: at constant pressure, second term: pressure influence), term three is the driving force due to a superficial viscous flow resulting from a gradient in the total pressure p (Pa) and the fourth term represents the electrostatic force acting on charged species due to a gradient of the elec-

tric potential field ϕ (V) (migration). On the right hand side are two terms describing friction forces: the sum accounts for the friction between species j and all other mobile species i (x are mole fractions, n are flux densities in (mol m^{-2} s^{-1})), and the second term represents friction between species j and the (stationary) solid matrix (lower index "M").

The most important parameters in this equation are the binary Maxwell–Stefan diffusion coefficients Ð (m^2 s^{-1}). The lower indices denote the two respective species, an upper index "eff" means that this is an effective diffusion coefficient taking into account the porosity ε (–) and the tortuosity τ (–) of the solid matrix, while those diffusion coefficients without the index "eff" are valid for free space binary interactions. For a more detailed treatment of the binary diffusion coefficients refer to Appendix A.9. The other parameters of the presented form of the generalised Maxwell–Stefan equations are explained in the respective following sections and in the list of symbols.

The modeling concept is based upon a finite volume discretisation along only one spatial coordinate z. For finite volume element simulations it is well known, that the simultaneous treatment of diffusive fluxes and convective flow can lead to numerical problems if the viscous flow contribution in relation to the overall mass transport is high. To prevent such problems, the viscous flow term (term three on the left hand side) of Eq. (1) is skipped and the Maxwell–Stefan equation is formulated only for the individual driving forces acting on the species j (diffusion and migration)

$$-\frac{c_j}{RT}\left(\frac{\partial\mu_j}{\partial z}\right)_{T,p} - \frac{c_j}{RT}\bar{V}_j\frac{\partial p}{\partial z} - c_j z_j\frac{F}{RT}\frac{\partial\phi}{\partial z}$$
$$= \sum_{i \neq j}\frac{x_i j_j - x_j j_i}{Ð_{ij}^{eff}} + \frac{j_j}{Ð_{jM}^{eff}} \tag{2}$$

In Eq. (2) in the friction terms on the right hand side not the overall flux densities n_j appear but only the individual flux densities j_j.

The overall flux densities are then calculated from the individual flux densities and an additive term for the pressure-driven convective contribution:

$$n_j = j_j + \tilde{c}_j v_p. \tag{3}$$

Here not the molar concentration with respect to the volume of the fluid phase, c (mol m^{-3}), is used, but a modified concentration $\tilde{c}$ (mol m^{-3}) with respect to the total volume including the porous matrix. v_p is the convective velocity (m s^{-1}), which is a function of the total pressure gradient according to Darcy's law:

$$v_p = -\frac{B_0}{\eta^{vis}}\frac{\partial p}{\partial z}. \tag{4}$$

The parameters are the dynamic viscosity η^{vis} (Pa s) of the mixture and the hydraulic permeability coefficient B^0 (m^2). The latter has to be determined experimentally, but for some simple geometries correlations are known. The simplest case

is the flow through parallel straight tubular pores (Poiseuille flow):

$$B_0 = \frac{d_{\text{pore}}^2}{32}. \tag{5}$$

In the following, this (simplifying) approach will be used.

In the implementation of the transport equations for a spatially discretised model, an upwind scheme is used which always uses the "upwind" concentrations, i.e. the concentrations in the left or the right neighbouring control volume depending on the direction of the convective flux, to calculate the convective contribution to the molar flux densities.

Using the overall flux densities, the general form of the component mass balances is

$$\frac{\partial c_j}{\partial t} = -\frac{\partial n_j}{\partial z} + \sum_k (r_k \cdot v_{j,k}) \tag{6}$$

with the reaction rates r_k of all occurring (electro-) chemical reactions (mol m^{-3} s^{-1}) and the stoichiometric coefficients $v_{j,k}$ (–) of component i in reaction k.

Finally a total mass balance can be formulated based on the continuity equation:

$$\frac{\partial \rho}{\partial t} = -\frac{\partial}{\partial z}(\rho v) \tag{7}$$

where ρ (kg m^{-3}) is the fluid mixture density and v (m s^{-1}) is the mean (superficial) mixture velocity. For compressible fluids the relation between pressure and density at constant entropy (which is the case for moderate pressures as typical for DMFC operation) is given by

$$\left(\frac{\partial p}{\partial \rho}\right)_S = v_{\text{sound}}^2 \tag{8}$$

where v_{sound} (m s^{-1}) is the speed of sound in the fluid (see Appendix A) and p (Pa) is the local pressure.

Finally, the product of mean mixture density and mean velocity is the total mass flux density (kg m^{-2} s^{-1}):

$$m_{\text{tot}} = \rho v \tag{9}$$

Combining Eqs. (7)–(9) one can formulate the total mass balance in terms of the pressure as variable, and its time derivative as a function of the total mass flux density:

$$\frac{\partial p}{\partial t} = -v_{\text{sound}}^2 \frac{\partial m_{\text{tot}}}{\partial z}. \tag{10}$$

In the simulation, the total mass flux density is calculated simply as the sum of the component mass flux densities, which in turn are the products of the molar flux densities and the respective molecular weights $\bar{M}_j$ (kg mol^{-1}):

$$m_{\text{tot}} = \sum_j n_j \bar{M}_j. \tag{11}$$

3.3. Energy transport and balancing

Within the DMFC, not only a variety of different mass transport phenomena occur simultaneously. The same is true for energy transport and production. As the DMFC consists of porous layers in which mobile species are transported, energy transport can take place both due to transport bound to the moving species and thermal conduction. The latter takes place in the mobile phase as well as in the stationary solid matrices in the different layers. Additionally, chemical and electrochemical reactions take place in the catalyst layers (AC) and (CC), and finally within the membrane (M) a spatially distributed heat production, Joule heating, occurs, due to the transport of charged species in an electric field.

To get a most simple model description of all these phenomena, it makes sense to formulate two independent energy flux densities: enthalpy flux densities

$$e = \sum_j e_j = \sum_j n_j h_j(T) \tag{12}$$

(J m^{-2} s^{-1}), which are coupled to the mass flux densities n_j (mol m^{-2} s^{-1}) of the mobile species and their specific enthalpies h_j (J mol^{-1}), and heat flux densities

$$q = -\lambda^{\text{eff}} \frac{\partial T}{\partial z} \tag{13}$$

(J m^{-2} s^{-1}) due to thermal conduction (Fourier law).

In Eq. (13) λ^{eff} (W m^{-1} K^{-1}) stands for the local effective thermal conductivity coefficient. The upper index "eff" denotes that it is dealt with a mixture of a fluid and a solid-phase, which both contribute to the thermal conduction. The effective thermal conductivity has to be calculated from the thermal conductivities of both phases taking into account their volume fractions. These calculations can be found in Appendix C.

The specific enthalpies of the mobile species are calculated from the specific enthalpies of formation, $\Delta_F H_j$, and the mean heat capacities $C_{p,j}$:

$$h_j = \Delta_F H_j^\theta + \int_{T^\theta}^{T} C_{p,j}(T)\,\mathrm{d}T \approx \Delta_F H_j^\theta + (T - T^\theta) \cdot C_{p,j} \tag{14}$$

By using enthalpy fluxes, all heats of reactions are accounted for automatically without the need for a heat production term in the energy balances of the respective DMFC layers.

Finally, Joule heating e_{Joule} (W m^{-3}) due to charge transport is described by the general equation

$$e_{\text{Joule}} = i \frac{\partial \phi}{\partial z}, \tag{15}$$

(W m^{-3}). It is always positive and independent of the direction of the charge flux.

Combining all three energy flux densities yields the general energy balance:

$$\frac{\partial T}{\partial t} = \frac{1}{\widetilde{(\rho c_p)}} \left[-\frac{\partial e}{\partial z} - \frac{\partial q}{\partial z} + e_{\text{Joule}} \right].$$ (16)

The local effective volumetric heat capacities $\widetilde{(\rho c_p)}$ are caclulated from the local porosities, concentrations and heat capacities of the present components. The calculation is presented in Appendix D.

3.4. Charge transport and balancing

Charge transport in the DMFC is bound to protons within the membrane material (proton conductor) and electrons in the electrical circuit (electron conductor). Therefore, the charge flux density i (A m^{-2}) within the proton conductor is coupled to the molar flux density of protons by Faradays law (z^* = number of single charges exchanged per molecule):

$$i = z^*_{H^+} F n_{H^+} = F n_{H^+}.$$ (17)

Charge production/consumption due to electrochemical reactions is similarly linked to the reaction rates with respect to the pore volume, r_k (mol m^{-3} s^{-1}), of the respective electrochemical reactions (as function of the respective overpotential η (V)):

$$i_k(\eta) = z_{H^+} F \nu_{H^+,k} r_k(\eta) \frac{V^{\text{pores}}}{A^S}.$$ (18)

In both, the membrane and the catalyst layers, charge balances have to be formulated accounting for the outer electrical cell current density i_{cell} (A m^{-2}) as well as for the above mentioned current densities resulting from proton flux in the membrane and the charge production in both catalyst layers. The general form of the charge balances is

$$\frac{\partial \tilde{Q}}{\partial t} = -\frac{\partial i}{\partial z} + \Gamma(\eta)$$ (19)

where $\tilde{Q}$ is the volumetric charge density (C m^{-3}) and Γ is the volumetric charge production (C m^{-3} s^{-1}) by electrochemical reactions:

$$\Gamma(\eta) = \sum_k i_k(\eta).$$ (20)

Simplifyingly it is assumed that the charge balances are fast compared to all other balances (material and energy) which leads to quasi-stationary formulations. In the catalyst layers, when balancing the electrons, only the charge flux to or from the adjacent diffusion layer (electron conductor) occurs, which is the cell current density i_{cell}. Within the catalyst layers electrons are produced or consumed by the electrochemical reactions as described above. Therefore, the final quasi-stationary charge balances have the form:

$$0 = i_{\text{cell}} - \sum_k i_k(\eta).$$ (21)

In the PEM no charge production occurs and local electroneutrality is assumed, therefore one ends up with the quasi-stationary charge balance:

$$0 = -\frac{\partial i^M}{\partial z}.$$ (22)

3.5. Overpotentials and cell voltage

For the formulation of rate equations for the electrochemical electrode reactions, one needs a definition for the electrode overpotentials, which is given by:

$$\eta = \Delta \phi - \Delta \phi^\theta_{i=0}$$ (23)

The overpotentials η (V) are defined as the difference between the real electrode potential $\Delta \phi$ (V) (w.r.t. standard hydrogen electrode) and that at open circuit condition (i.e. no cell current, $i = 0$) and thermodynamic standard conditions (pressure 10^5 Pa, temperature 298 K, all reactants activities equal one, upper index θ). For the DMFC the following values can be found in the literature:

Anodic methanol oxidation:

$$\Delta \phi^\theta_{a,i=0} = 0.02 \text{ V}$$ (24)

Cathodic oxygen reduction:

$$\Delta \phi^\theta_{c,i=0} = 1.23 \text{V}$$ (25)

Then the cell voltage can be calculated from the reversible open circuit cell voltage at the above mentioned standard conditions ($U^\theta_{\text{cell},i=0} \approx 1.21$V), the anode and cathode overpotentials, η_a and η_c (V), respectively, and the Ohmic losses within the membrane represented by the total difference in the polymer-phase electrical potentials $\Delta \phi^M$ (V):

$$U_{\text{cell}} = U^\theta_{\text{cell},i=0} - \eta_a + \eta_c - \Delta \phi^M.$$ (26)

3.6. Anode compartment (A)

The anode compartment is assumed to be a spatially concentrated phase element (ideally mixed, CSTR behaviour). It has one inlet (feed, index AF) and one outlet, and it is connected to the anode diffusion layer (AD). Fresh water methanol solution is fed at the inlet, with a supposedly very low carbon dioxide content. Methanol and water are transported through the anode diffusion layer towards the anode catalyst, while produced carbon dioxide is transported in the opposite direction to leave the diffusion layer into (A), and on this way being removed through the anode outlet (see Fig. 3). The material balances are:

$$\frac{dc_j^A}{dt} = \frac{1}{V^A}(F^{AF} c_j^{AF} - F^A c_j^A + A^S n_j^{AD}(z^{AD} = 0))$$

$$\approx \frac{1}{V^A}(F^{AF}(c_j^{AF} - c_j^A) + A^S n_j^{AD}(z^{AD} = 0))$$ (27)

with j = H$_2$O, CH$_3$OH, CO$_2$. In Eq. (27) F^{AF} is the feed volume flow rate (m^3 s^{-1}), V^A is the total volume of the

channels (m^3), c_j^{AF} are the feed concentrations (mol m^{-3}) and F^A is the outlet volume flow rate ($m^3 s^{-1}$). The difference between the two flow rates F^{AF} and F^A can be assumed to be small, therefore it is neglected which results in the simplified formulation given in the second line of Eq. (27).

The anode pressure p^A as well as the temperature T^A are given as input parameters which are known from the experiments. Therefore, no total mass and energy balances are formulated here.

3.7. Cathode compartment (C)

The cathode compartment's structure is similar to that of the anode compartment. The inlet is fed with air with the components oxygen, nitrogen (including all other inert gases), water and carbon dioxide. Oxygen enters the cathode diffusion layer (CD) while water and carbon dioxide produced in the cathode catalyst layer (CC) are transported out of the DMFC (see Fig. 3)

The material balances are:

$$\frac{dc_j^C}{dt} = \frac{1}{V^C}(F^{CF}c_j^{CF} - F^C c_j^C + A^S n_j^{CD}(z^{CD} = d^{CD})) \quad (28)$$

with $j = N_2, O_2, H_2O, CO_2$.

Here F^{CF} is the feed volume flow rate ($m^3 s^{-1}$), V^C is the total volume of the channels (m^3), c_j^{CF} are the feed concentrations (mol m^{-3}) and F^C is the outlet volume flow rate ($m^3 s^{-1}$). The latter can be calculated from the inlet flow rate and the molar fluxes exchanged with the diffusion layer (CD) (quasi-stationary total material balance):

$$F^C = F^{CF} + \frac{RT^C}{p^C}A^S \sum_j n_j^{CD}(z^{CD} = d^{CD}) \quad (29)$$

with $j = N_2, O_2, H_2O, CO_2$.

The cathode pressure p^C as well as the gas and the bipolar plate temperatures, T^C and T_{carbon}^C, respectively (explanation for two temperatures in Section 3.9), are input parameters known from experiments. Therefore, as in (A), no energy and no total mass balances are necessary.

3.8. Anode diffusion layer (AD)

The anode diffusion layer connects the anode compartment (A) and the anode catalyst layer (AC) (see Fig. 3). It consists of a chemically inert carbon fibre material coated with a certain amount of PTFE (20–25 wt.%). It supplies educts (methanol and water) to the anode catalyst and removes the carbon dioxide from there. It also collects the electrons from the anode reaction and ensures good electric contact with the bipolar plate (current collector). All fluxes are assumed to occur only perpendicular to the surface plane (i.e. in z-direction). Data about porosity and other physical parameters are given in Appendix B.

It is assumed that the complete pore space is filled with liquid methanol–water solution and soluted carbon dioxide. Formation of a gas phase from carbon dioxide is neglected (see assumptions in Section 3.1).

For the three species water (H_2O), methanol (CH_3OH) and carbon dioxide (CO_2), the material balances (formulated in molar concentrations) are:

$$\frac{\partial c_j^{AD}}{\partial t} = -\frac{1}{\varepsilon_{pores}^{AD}}\frac{\partial n_j^{AD}}{\partial z} \quad (30)$$

with $j = H_2O, CH_3OH, CO_2$

The total mass balance, analogue to Eq. (10), is given by

$$\frac{\partial p^{AD}}{\partial t} = -(v_{sound}^{AD})^2\frac{\partial m_{tot}^{AD}}{\partial z}. \quad (31)$$

Finally, the energy balance is

$$\frac{\partial T^{AD}}{\partial t} = -\frac{1}{(\widetilde{(\rho c_p)})^{AD}}\left(\frac{\partial e^{AD}}{\partial z} + \frac{\partial q^{AD}}{\partial z}\right), \quad (32)$$

analogue to Eq. (16), but Joule heating due to electron transport is neglected as the Ohmic resistance (and therefore the electric potential gradient) in the carbon paper can be assumed to be negligible.

In Eq. (32) the molar mixture heat capacity $(\widetilde{\rho c_p})^{AD}$ is approximated by the value for pure water (see Appendix D). e^{AD} represents the sum of the enthalpy flux densities connected with the material fluxes and q^{AD} is the heat flux density due to thermal conduction in the liquid mixture and the pore walls (carbon fibres).

For constant activity coefficients and pure liquid-phase the Maxwell–Stefan mass transport equation, Eq. (2). simplifies to:

$$-c_{tot}^{AD}\frac{\partial x_j^{AD}}{\partial z} = \sum_{i \neq j}\frac{x_i^{AD}j_j^{AD} - x_j^{AD}j_i^{AD}}{Đ_{ij}^{AD,eff}} + \frac{j_j^{AD}}{Đ_{jM}^{AD,eff}} \quad (33)$$

with $j = H_2O, CH_3OH, CO_2$.

The total concentration c_{tot}^{AD} (mol m^{-3}) is the sum of all species concentrations:

$$c_{tot}^{AD} = \sum_j c_j^{AD} \quad (34)$$

with $j = H_2O, CH_3OH, CO_2$

As demonstrated by Krishna and Wesselingh [18], this flux-implicit set of transport equations can be transformed to get explicit formulations for the flux densities:

$$(j^{AD}) = -c_{tot}^{AD}[B^{AD}]^{-1}\nabla(x^{AD}) \quad (35)$$

where the elements of the transport matrix $[B^{AD}]$ are:

diagonal elements : $B_{ii}^{AD} = \frac{1}{Đ_{iM}^{AD,eff}} + \sum_{k \neq i}\frac{x_k^{AD}}{Đ_{ik}^{AD,eff}}, \quad (36)$

all other elements : $B_{ij(i \neq j)}^{AD} = -\frac{x_i^{AD}}{Đ_{ij}^{AD,eff}}. \quad (37)$

Pressure-driven convective transport is described separately by adding a term to the diffusion flux densities to get the overall molar flux densities n_j^{AD} (mol m^{-2} s^{-1}), analogue to Eq. (3):

$$n_j^{AD} = j_j^{AD} + \tilde{c}_j^{AD} v_p^{AD} \qquad (38)$$

with $j = H_2O, CH_3OH, CO_2$.

The convective velocity v_p^{AD} (m s^{-1}) is calculated as presented in Section 3.2 (Eqs. (4) and (5)). As the carbon dioxide and methanol concentrations in the liquid mixture in (AD) are small compared to the water concentration, for the dynamic viscosity as function of local temperature and pressure a correlation for pure water is used (calculation see Appendix A.5).

The binary diffusion coefficients related to species-species interaction were determined from literature correlations (see Appendix A.9). The binary diffusion coefficients related to species–matrix interaction are unknown. But for liquid-phase transport in large pores (in the diffusion layers the pore diameters are in the order of 10–100 μm) species–matrix interactions are small compared to the species–species interactions for diffusive transport. But simply skipping the terms with the species–matrix binary diffusion coefficients in Eq. (36) leads to numerical problems, as the resulting transport matrix $[B^{AD}]$ can not be inverted by MatLab due to ill conditioning (too close to singular). Therefore, the values for the binary species–matrix diffusion coefficients were set to values which are three orders of magnitude higher than those of the species–species interactions. Thus, the numerical problem were solved while the influence of the wall friction on the individual flux densities j_{jF}^{AD} becomes negligible.

The total mass flux densities, enthalpy flux densities and conductive heat flux densities are calculated as described in Sections 3.2 and 3.3

3.9. Cathode diffusion layer (CD)

Material and energy balances are formulated analogue to (AD). The mobile species are oxygen (O_2), nitrogen (N^2), water (H_2O) and carbon dioxide (CO_2).

The major difference to (AD) results from the fact, that here the mixture is an ideal gas and not a liquid. Therefore, no total mass balance is needed and the local total pressure p^{CD} is given by the sum of the local partial pressures p_j^{CD} (Pa):

$$p^{CD} = \sum_j p_j^{CD} = RT^{CD} \sum_j c_j^{CD} \qquad (39)$$

with $j = N_2, O_2, H_2O, CO_2$.

For diffusive one-dimensional mass transport in a mixture of ideal gases, the Maxwell–Stefan Eq. (2) simplifies to:

$$-\frac{1}{RT^{CD}} \frac{\partial p_j^{CD}}{\partial z} = \sum_{i \neq j} \frac{y_i^{CD} j_j^{CD} - y_j^{CD} j_i^{CD}}{Đ_{ij}^{CD,eff}} + \frac{j_j^{CD}}{Đ_{jM}^{CD,eff}} \qquad (40)$$

with $j = N_2, O_2, H_2O, CO_2$; where j_j^{CD} are the diffusive mass flux densities in (mol m-2 s^{-1}) and y_j^{CD} are the gas mole fractions.

The binary diffusion coefficients can be easily and quite reliably derived from several correlations (see Appendix A.9) or alternatively from the kinetic gas theory. The species–matrix diffusion coefficients are calculated using the equation for Knudsen diffusion:

$$Đ_{jM}^{CD,eff} = \frac{\varepsilon_{pores}^{CD}}{\tau^{CD}} \frac{d_{pore}^{CD}}{3} \sqrt{\frac{8RT^{CD}}{\pi \bar{M}_j}} \qquad (41)$$

with $j = N_2, O_2, H_2O, CO_2$.

In Eq. (41) $\bar{M}_j$ are the molecular weights (kg mol^{-1}) and d_{pore}^{CD} (m) is the mean pore diameter in the matrix.

The mass flux densities can be obtained from the transport equations following the same numerical method as described for (AD). Also the calculation of the total mass, enthalpy and heat flux densities is analogous. Only one major difference to the anode side has to be accounted for. On the anode side, a liquid mixture (mainly water) is pumped through the channels of (A). Due to the high heat capacity of water and the relatively high heat transfer coefficients between the liquid mixture and the channel walls, a uniform temperature T^A can be assumed. On the cathode side the situation is totally different in this respect, as the gas mixture has a heat capacity of only

$$(\rho c_p)_{air} \approx 1.3 \frac{kg}{m^3} \cdot 1010 \frac{J}{kg\,K} \approx 1300 \frac{J}{m^3\,K} \qquad (42)$$

which is negligible compared to that of the bipolar plate

$$(\rho c_p)_{graphite} \approx 2000 \frac{kg}{m^3} \cdot 711 \frac{J}{kg\,K} \approx 1.422 \cdot 10^6 \frac{J}{m^3\,K}. \qquad (43)$$

The effect of this situation, observed in the experiments, is that the air pumped through the cathode bipolar plate changes its temperature only marginally (around 1–2 K maximum, see also basic model assumptions) and remains at 30–35 °C, while the temperature of the bipolar plate is nearly the same as that on the anode side (up to 90 °C in the presented experiments). Thermal energy is transported with low resistance through the planar contact areas at the outer gaskets and through the solid materials of the MEA. Therefore, on the cathode side, two temperatures have to be accounted for as boundary/operating conditions: The gas temperature, which nearly equals the feed temperature T^C (simplifyingly assumed to be equal), and the solid temperature T_{carbon}^C. For the calculation of the enthalpy flux (convective heat flux) between (CD) and (C), the gas temperatures have to be accounted for, as the gases are the mobile species. For the calculation of the conductive heat flux, the temperatures of the solid matrices have to be used, as thermal conduction through

the gas-phase can be neglected in comparison to that through the solid materials.

But this distinction is only necessary for the energy fluxes between (CD) and (C). Within the diffusion layer (CD) still a uniform temperature valid for gas and solid matrix can be assumed, as here the flow velocity is some orders of magnitude lower as in the gas channels of (C) and due to the small pore diameters and high pore tortuosity an intense heat exchange between gas and solid can be expected. Therefore, the temperature can also be expected to show only a slight slope within (CD), whereas at the interface between (CD) and the gas channels in (C) it can change dramatically, depending on the cathode and anode feed temperatures.

3.10. Membrane electrode assembly

The MEA consists of the polymer electrolyte membrane (M) and the anode and cathode catalyst layers (AD) and (CD), respectively. These three layers are highly interconnected by the proton-conducting membrane material content within the catalyst layers, therefore they can not be treated separately. Strains of polymer material are running through the catalyst layers, connecting catalyst particles to the membrane on the ionic conductor level. These strains not only form an ionic connection for mobile protons to the membrane (M), but also with respect to all species which can enter the pores within this material. In the case of NAFION™ these species are water and methanol, whereas the membrane is assumed to be impermeable for all gases (carbon dioxide, oxygen, nitrogen). This assumption is justified by the fact that the maximum content of these gases in the pore fluid of the membrane is limited by their solubility in water (and methanol), which is very low, especially at high operating temperatures.

As the pore volume of the polymer-phase within the catalyst layers is small compared to its surface open to the free pores within the catalyst layers, it will be furthermore assumed that, at this interface between the catalyst layers and the membrane, phase equilibrium is always established.

On the anode side, the phase equilibrium can be described applying a UNIFAC activity model [19] for the liquid in the free pores of (AC), and a Flory–Huggins activity model [17,20] for the liquid inside the polymer-phase (for a detailed description see [15]). In the latter, the activity of a species j is given as a function of the volume fractions ε_j of all mobile species and the polymer backbone, treating the polymer backbone and the mobile species as a liquid mixture (typical polymers are undercooled liquids):

$$
a_j = \varepsilon_j \exp \left\{ \sum_{i \neq j} \left[\left(1 - \frac{\bar{V}_j}{\bar{V}_i} \right) \varepsilon_i + \chi_{j,i} \varepsilon_i^2 \right] \right.
$$
$$
\left. + \frac{\bar{V}_j}{2 \cdot N_{M,cu} \cdot \bar{V}_{M,cu}} \varepsilon_M^{1/3} \right\}. \tag{44}
$$

In Eq. (44) for the polymer material the lower index "M" is used. For each pair of species, a non-ideality parameter $\chi_{j,i}$ is required. Crosslinking of the polymer material is accounted for in the last term on the right hand side: $N_{M,cu}$ is the number of sequential single polymer chain units (i.e. monomer units) within the main polymer chain between two crosslinks, $\bar{V}_{M,cu}$ is the molar volume of such a single chain unit in (m³ mol⁻¹). As the molar volume of the polymer is some orders of magnitude higher than those of the mobile species, the term $(1 - \bar{V}_j/\bar{V}_i)$ is approximately 1. In the following, three species are accounted for: The polymer backbone, water and methanol. Therefore, three non-ideality parameters are needed, which were determined from swelling experiments [15] as

$$
\chi_{H_2O,M} = 0.7177, \ \chi_{CH_3OH,M} = 0.1348 \text{ and } \chi_{H_2O,CH_3OH} = 1.3.
$$

The protons, strictly speaking, are also a mobile species, but they are treated separately, as will be presented later.

The anode phase equilibrium for water and methanol, obtained from a dynamic mass balance model using both, UNIFAC and Flory–Huggins activity models, can be approximated by the following fitting functions for (AC) pore methanol mole fractions below 0.03 (i.e. typical operation range of a DMFC) [15]:

$$
\varepsilon_{CH_3OH}^{ACP} = 25.4831 \cdot (x_{CH_3OH}^{AC})^3 + 4.2821 \cdot (x_{CH_3OH}^{AC})^2
$$
$$
+ 1.6354 \cdot x_{CH_3OH}^{AC} \tag{45}
$$

$$
\varepsilon_{H_2O}^{ACP} = -104.9956 \cdot (x_{CH_3OH}^{AC})^3 + 20.9052 \cdot (x_{CH_3OH}^{AC})^2
$$
$$
+ 2.6349 \cdot x_{CH_3OH}^{AC} + 0.4601 \tag{46}
$$

The temperature influence was found to be negligible: Activity coefficients predicted from the UNIFAC model for this system show only a weak temperature dependence, and in the Flory–Huggins model temperature influences only the molar volumes, which are also nearly independent of temperature for liquids.

A second phase equilibrium model has to be formulated for the interface between the membrane (M) and the cathode catalyst layer (CC) pores. Here it is assumed, that in the pores of (CC) a gas-phase is predominant (i.e. condensation of water is neglected). Experimental data are available from the literature (e.g. [21,22]) for the equilibrium relative water content of NAFION™ (with respect to the number of fixed sulfonic acid groups –SO₃⁻):

$$
\Lambda^M = \frac{N_{H_2O}^M}{N_{R-SO_3^-}}. \tag{47}
$$

as function of the "water vapour activity" (ideal gas, defined as in the references [21,22]):

$$
a_{H_2O(g)}^* = \frac{p_{H_2O}}{p_{H_2O}^{sat}(T)}. \tag{48}
$$

It is possible to fit a polynomial to these data describing the phase equilibrium here [15]:

$$\Lambda^{CCP} = 28.5 \cdot (a_{H_2O(g)}^{*,CC} - 0.35)^3$$
$$+ 5 \cdot (a_{H_2O(g)}^{*,CC} - 0.35) + 3 \qquad (49)$$

with

$$a_{H_2O(g)}^{*,CC} = \frac{p_{H_2O}^{CC}}{p_{H_2O}^{sat}(T^{CC})}. \qquad (50)$$

Finally some attention is paid to viscous flow in the membrane material. As the pores within NAFION™ are extremely small (in the range of a few nanometers) the question arises whether small pressure differences over the DMFC (typically maximum 2 bars) can lead to a significant viscous flow contribution. This question can be addressed by some simple calculations [15]. The outcome is, that a pressure difference of roughly $\Delta p^M \approx 25$ bars would be required to obtain water crossover fluxes of the order of magnitude, which was observed in the experiments. As in real DMFC operation the maximum pressure differences do not exceed 1–2 bars, one can conclude that viscous flow can only contribute a few percent to the measured membrane crossover fluxes. Therefore, it is justified to neglect pressure-driven flow in the membrane model.

3.10.1. Anode catalyst layer (AC)

In the anode catalyst layer one finds several phases which are highly interconnected: free pores, polymer-phase and electron conductor. Water, methanol and carbon dioxide are the mobile species within the free pores. The catalyst layers are modelled as concentrated parameter systems. The species mass balances of (AC) are given by:

$$\frac{dc_j^{AC}}{dt} = \frac{n_j^{AD}(z^{AD} = d^{AD}) - n_j^M(z^M = 0)}{\varepsilon_{pores}^{AC} d^{AC}} + v_{a,j} r_a \qquad (51)$$

with $j = H_2O, CH_3OH, CO_2$ and the stoichiometric coefficients of the anodic electrochemical methanol oxidation:

$$v_{a,CH_3OH} = -1 \quad v_{a,H_2O} = -1$$
$$v_{a,CO_2} = +1 \quad v_{a,H^+} = +6 \qquad (52)$$

The rate of the electrochemical methanol oxidation is formulated as a Butler–Volmer equation:

$$r_a = k_a \left[x_{CH_3OH}^{AC} \exp\left(\frac{\alpha_a 6F}{RT^{AC}} \eta_a \right) \right.$$
$$\left. - x_{CO_2}^{AC} \exp\left(-\frac{(1 - \alpha_a)6F}{RT^{AC}} \eta_a \right) \right]. \qquad (53)$$

In Eq. (53) k_a is the rate constant (mol m^{-3} s^{-1}) (value for simulation: $k_a = 6 \times 10^{-3}$ mol m^{-3} s^{-1}), α_a is the charge transfer coefficient (set to $\alpha_a = 0.1$) and η_a is the anode overpotential (V). The water mole fraction is not included in Eq. (53) due to the fact that it can be assumed to be close to unity

and is not changing significantly. Due to the very complex reaction mechanism this rate equation can of course be only a first approach. More realistic models of the reaction kinetics have to account for methanol oxidation reaction intermediates and adsorption and desorption phenomena on the binary anode catalyst. Such more detailed kinetic models were e.g. proposed in [1,2], but the number of free model parameters to be determined is considerable, as is the increase in required computation time.

The concentrations of water and methanol in the polymer-phase within (A) (denoted as ACP) are calculated assuming phase equilibrium with the pores in (AC), as described above (Section 3.10).

The total mass balance in (AC) is given by

$$\frac{dp^{AC}}{dt} = -\frac{v_{sound}^2}{d^{AC}} \left(m_{tot}^M(z^M = 0) - m_{tot}(z^{AD} = d^{AD}) \right) \qquad (54)$$

As the cell is operated galvanostatically (i.e. the cell current density i_{cell} is a known operating parameter), the charge balance can be formulated quasi-stationary:

$$0 = i_{cell} - i^M(z^M = 0). \qquad (55)$$

Due to the quasi-stationarity of the charge balance, the mass and charge balances are not coupled. Therefore, the current density of the anodic reaction, i_a, expressed in terms of the anodic rate expression, Eq. (53), is identical to the known cell current density:

$$i_a = d^{AC} \cdot \varepsilon_{pores}^{AC} \cdot 6 \cdot F \cdot r_a(\eta_a) = i_{cell}. \qquad (56)$$

From Eq. (56) and the anodic rate expression, Eq. (53), the anode overpotential can be calculated numerically by recursion.

Finally, the energy flux densities at the interfaces between (AC) and (AD) and (AC) and (M), respectively, are accounted for in the energy balance of (AC):

$$\frac{dt^{AC}}{dt} = -\frac{\begin{aligned}&((e^M(z^M = 0) - e^{AD}(z^{AD} = d^{AD})) \\ &+ (q^M(z^M = 0) - q^{AD}(z^{AD} = d^{AD})))\end{aligned}}{(\widetilde{\rho c_p})^{AC} d^{AC}}. \qquad (57)$$

### 3.10.2. Cathode catalyst layer (CC)

Very similar to (AC) also in (CC) spatially concentrated balances for mass, charge and energy are formulated. The mass balances for oxygen, nitrogen, water vapour and carbon dioxide in terms of molar concentrations are:

$$\frac{dc_j^{CC}}{dt} = \frac{n_j^M(z^M = d^M) - n_j^{CD}(z^M = 0)}{\varepsilon_{pores}^{CC} d^{CC}}$$
$$+ v_{c,j} r_c + v_{cross,j} r_{cross} \qquad (58)$$

with $j = N_2, O_2, H_2O, CO_2$

In Eq. (58) not only the desired electrochemical oxygen reduction has to be accounted for, but also the undesired direct methanol oxidation:

(a) Oxygen reduction (consumes H^+ and e^-):

$$1.5\,O_2 + 6H^+ + 6e^- \rightarrow 3H_2O \tag{59}$$
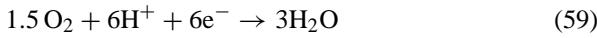
(b) Methanol oxidation (produces H^+ and e^-):

$$CH_3OH + 0.5O_2 \rightarrow CO_2 + 4H^+ + 4e^- \tag{60}$$
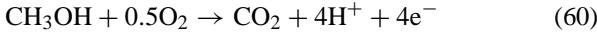
The stoichiometric coefficients of these reactions are

$$\nu_{c,O_2} = -1.5 \quad \nu_{c,N_2} = 0 \quad \nu_{c,H_2O} = +3$$

$$\nu_{c,CO_2} = 0 \quad \nu_{c,H^+} = -6$$

and

$$\nu_{cross,O_2} = -0.5 \quad \nu_{cross,N_2} = 0 \quad \nu_{cross,H_2O} = 0$$

$$\nu_{cross,CO_2} = +1 \quad \nu_{cross,H^+} = +4.$$

It is known that the reaction mechanism of the electrochemical oxygen reduction is complicated with several possible intermediates. However, as in (AC), in order to keep the number of unknown parameters small, again a Butler–Volmer type equation is applied:

$$r_c = k_c \left[\left(\frac{p_{O_2}^{CC}}{10^5\,\text{Pa}} \right)^{1.5} \exp\left(-\frac{\alpha_c 6F}{RT^{CC}} \eta_c \right) \right.$$
$$\left. - \exp\left(-\frac{(1-\alpha_c)6F}{RT^{CC}} \eta_c \right) \right]. \tag{61}$$

In Eq. (61) k_c is the rate constant $(\text{mol m}^{-3}\,\text{s}^{-1})$ (value for simulation: $k_c = 1.27 \times 10^{-21}\,\text{mol m}^{-3}\,\text{s}^{-1}$), α_c is the charge transfer coefficient (set to $\alpha_c = 0.5$) and η_c is the cathode overpotential (V).

Methanol is assumed to be immediately consumed when coming into contact with the cathode. Therefore, its concentration in (CCP) and (CC) drops to zero. Under these conditions the rate of the direct oxidation of methanol at the cathode, r_{cross} is proportional to the methanol flux from (M) to (CC):

$$r_{cross} = \frac{n_{CH_3OH}^M(z^M = d^M)}{d^{CC}\varepsilon_{pores}^{CC}}. \tag{62}$$

The concentration of water in (CCP) is calculated from the equilibrium condition presented in Section 3.10.

The overall pressure p^{CC} is calculated from the concentrations of all four gas species c_j^{CC} according to the ideal gas law:

$$p^{CC} = RT^{CC} \sum_j c_j^{CC} \tag{63}$$

Following the same argumentation as for (AC), the total charge balance is formulated quasi-stationary, and is decoupled from the mass balances as the cell is operated galvanostatically:

$$0 = i_{cell} - i^M(z^M = d^M) \tag{64}$$

As at the cathode two electrochemical reactions take place simultaneously (oxygen reduction with the charge production rate r_c, and methanol oxidation with the charge production rate r_{cross}), a charge balance has to be formulated either for the electron or the proton conductor-phase. For the electron conductor phase this quasi-stationary charge balance is given by:

$$0 = i_{cell} + (i_{cross} + i_c). \tag{65}$$

In Eq. (65) the current density of the cathode oxygen reduction reaction is given by

$$i_c = d^{CC}\varepsilon_{pores}^{CC}6Fr_c \tag{66}$$

(6 exchanged electrons per net reaction) and the current density of the oxidation of crossover methanol analogous by

$$i_{cross} = d^{CC}\varepsilon_{pores}^{CC}4Fr_{cross}. \tag{67}$$

(4 exchanged electrons per net reaction). From Eqs. (65)–(67) together with the cathode rate expression, Eq. (61), the cathode overpotential η_c can be determined numerically in a recursion, similar to the anode overpotential.

Finally, analogue to (AC), the energy balance for (CC) is formulated as:

$$\frac{dt^{CC}}{dt} = -\frac{\begin{array}{c}((e^{CD}(z^{CD} = 0) - e^M(z^M = d^M))\\ + (q^{CD}(z^{CD} = 0) - q^M(z^M = d^M)))\end{array}}{(\widetilde{\rho c_p})^{CC}d^{CC}}. \tag{68}$$

3.10.3. Polymer electrolyte membrane (M)

The PEM (M) is a one-dimensional transport element like the diffusion layers (AD) and (CD). The mass balances for water and methanol are given by:

$$\frac{\partial c_j^M}{\partial t} = -\frac{\partial n_j^M}{\partial z} \tag{69}$$

with $j = H_2O, CH_3OH$.

But the material structure and the occurring physical phenomena are much more complex. The PEM has not a constant porosity, but one that strongly depends on the local water and methanol content. The relative water content Λ, Eq. (47), can have values between $\Lambda = 0$ (totally dry membrane) and $\Lambda \approx 30$ (fully swollen with water and methanol at room temperature), depending on temperature and other conditions. Different water and methanol contents result in different degrees of swelling, and therefore different thicknesses and porosities. Therefore, it is not suitable to formulate mass balances in molar concentrations, as these refer to a constant overall volume. It is more convenient to use a concentration measure which refers to the constant cross-sectional area of the cell, A^S (m^2). This molar density $\hat{N}_j$ (mol m^{-2}) is defined as quotient of the total molar amount of species j, N_j (mol), and the cell cross-sectional area:

$$\hat{N}_j = \frac{N_j}{A^S}. \tag{70}$$

For the mass transport equations (see below) a variety of other concentration measures are needed. The necessary conversions are given in Appendix E.

Using this introduced molar density, the mass balances for the control volumes (index k) in the discretised model have the form

$$\frac{d\hat{N}_{j,k}^{M}}{dt} = n_{j,k}^{M} - n_{j,k+1}^{M} \tag{71}$$

with $j = H_2O, CH_3OH$.

In Eq. (71), swelling of the membrane is assumed to be in the steady state. A total mass balance is not formulated, as pressures are not discussed within the membrane.

The charge balance is considered in steady state (quasi-stationary):

$$0 = -\frac{\partial i^{M}}{\partial z}. \tag{72}$$

As the mass balances, the energy balance is quite similar to that in the diffusion layers. The only difference is that it has to account not only for convective and conductive heat fluxes, but also for Joule heating resulting from the electric resistance of the membrane caused by friction between mobile charged species and the immobilised counter charges at the pore walls. The heat production due to Joule heating, e_{Joule}^{M} ($J\,m^{-3}\,s^{-1}$), is proportional to the electric current density i^{M} and the gradient of the electric potential ϕ^{M}:

$$e_{Joule}^{M} = i^{M}\frac{\partial\phi^{M}}{\partial z}. \tag{73}$$

With all this, the energy balance finally is

$$\frac{\partial T^{M}}{\partial t} = \frac{1}{(\widetilde{\rho c_p})^{M}}\left[-\frac{\partial e^{M}}{\partial z} - \frac{\partial q^{M}}{\partial z} + i^{M}\frac{\partial\phi^{M}}{\partial z}\right]. \tag{74}$$

In the following, transport equations for mass and energy are formulated for (M). The charge transport is expressed in terms of the proton flux. Mass transport is described using the Maxwell–Stefan approach, as has already been done for the diffusion layers. But in the PEM, a more complex formulation of the driving forces has to be chosen. First, the migration term has to be included, as one of the mobile species (protons) is charged and an electric field is present within the membrane. Second, the diffusive term has to account for the highly non-ideal behaviour of the mobile

species within the membrane pores, i.e. the gradients of the chemical potentials have to be used as driving force, which are equal to the gradients in the species activities (calculated using the presented Flory–Huggins activity model). The pressure-dependency of the chemical potentials as well as viscous flow due to pressure differences across the membrane can be neglected as was shown in Section 3.10.

All this leaves the following form of the Maxwell–Stefan equations for the mobile species ($j = H^{+}, H_2O, CH_3OH$):

$$-c_{j}^{M}\frac{1}{a_{j}^{M}}\frac{\partial a_{j}^{M}}{\partial z} - z_{j}^{*}c_{j}^{M}\frac{F}{RT^{M}}\frac{\partial\phi^{M}}{\partial z}$$

$$= \sum_{i\neq j}\frac{x_{i}^{M}n_{j}^{M} - x_{j}^{M}n_{i}^{M}}{\text{Đ}_{ij}^{M,eff}} + \frac{n_{j}^{M}}{\text{Đ}_{jM}^{M,eff}} \tag{75}$$

In Eq. (75), as superficial viscous flow due to pressure gradients is not accounted for, the total molar flux densities n_i appear in the friction terms on the right hand side of the equation. Three of the six binary diffusion coefficients $\text{Đ}_{ij}^{M,eff}$ are taken from the literature [23] as a starting point, using the general expression

$$\text{Đ}_{ij}^{eff}(T, \Lambda^{M}) = \text{Đ}_{ij}^{\theta}\Lambda^{M}\exp\left[-\frac{E_{ij}^{A}}{R}\left(\frac{1}{T} - \frac{1}{T^{\theta}}\right)\right] \tag{76}$$

with the reference temperature $T^{\theta} = 298\,K$. The values of the standard diffusion coefficients and the activation energies are given in Table 2. The two additional binary diffusion coefficients for methanol/pore wall and methanol/protons are formulated in the same way, using the literature values for water/pore wall and water/protons as a first estimate, respectively. The coefficient for methanol/water is calculated using the free solution correlation of HAYDUK and MINHAS for solutes in aqueous solutions [34d]:

$$\text{Đ}_{CH_3OH,H_2O} \approx D_{CH_3OH,H_2O}^{\infty}$$

$$= 1.25\cdot10^{-12}(\bar{V}_{CH_3OH}^{-0.19} - 0.292)T^{1.52}(\eta_{H_2O}^{vis})^{\epsilon*} \tag{77}$$

with $\epsilon* = \dfrac{9.58}{\bar{V}_{CH_3OH}} - 1.12$.

All details on derivation of the binary diffusion coefficients are given in Appendix A.9.

Table 2
Parameters for calculation of binary diffusion coefficients in Nafion™ (M represents solid matrix/pore wall)

Species pair (i/j)	Original (* =[23]) parameters		Adjusted parameters	
	Đ_{ij}^{θ} ($m^2\,s^{-1}$)	E_{ij}^{A} (kJ mol^{-1})	Đ_{ij}^{θ} ($m^2\,s^{-1}$)	E_{ij}^{A} (kJ mol^{-1})
H_2O/H^{+}	0.85×10^{-10} (*)	10.54 (*)	0.15×10^{-10}	10.54
H_2O/M	0.55×10^{-11} (*)	20.25 (*)	0.20×10^{-11}	50.25
H^{+}/M	0.22×10^{-10} (*)	10.54 (*)	0.22×10^{-10}	10.54
CH_3OH/H^{+}	Identical to H_2O/H^{+}		0.60×10^{-10}	8.43
CH_3OH/M	Identical to H_2O/M		5.00×10^{-11}	25.13
CH_3OH/H_2O	1.25×10^{-12}	–	5.00×10^{-12}	–

As the flux density of protons $n_{H^+}^M$ is given by the electric current density i_{cell} using Faraday's law

$$n_{H^+}^M = \frac{i^M}{F} = \frac{i_{cell}}{F}, \tag{78}$$

only the flux densities of water and methanol have to be determined. In this case, the flux-implicit transport equations, Eq. (75), can be easily transformed into a flux-explicit form by rearranging:

$$n_{CH_3OH}^M = \frac{L_{H_2O} + L_{CH_3OH} - n_{H^+}L_1 - n_{H_2O}L_2}{L_3} \tag{79}$$

$$n_{H_2O}^M = \frac{\begin{array}{c} L_{H_2O} - n_{H^+}(L_4 - (L_1 L_6/L_3)) \\ - (L_2 + L_3)(L_6/L_3) \end{array}}{L_5 - (L_2 L_6/L_3)} \tag{80}$$

with

$$L_{H_2O} = -\frac{c_{H_2O}^M}{a_{H_2O}^M}\frac{\partial a_{H_2O}^M}{\partial z}, \tag{81}$$

$$L_{CH_3OH} = -\frac{c_{CH_3OH}^M}{a_{CH_3OH}^M}\frac{\partial a_{CH_3OH}^M}{\partial z}, \tag{82}$$

$$L_1 = -\frac{x_{H_2O}}{Ð_{H^+,H_2O}^{eff}} - \frac{x_{CH_3OH}}{Ð_{H^+,CH_3OH}^{eff}}, \tag{83}$$

$$L_2 = \frac{x_{H^+}}{Ð_{H^+,H_2O}^{eff}} + \frac{1}{Ð_{H_2O,M}^{eff}} \quad \text{and} \tag{84}$$

$$L_3 = \frac{x_{H^+}}{Ð_{H^+,CH_3OH}^{eff}} + \frac{1}{Ð_{CH_3OH,M}^{eff}}, \tag{85}$$

$$L_4 = -\frac{x_{H_2O}}{Ð_{H^+,H_2O}^{eff}}, \tag{86}$$

$$L_5 = \frac{x_{H^+}}{Ð_{H^+,H_2O}^{eff}} + \frac{x_{CH_3OH}}{Ð_{H_2O,CH_3OH}^{eff}} + \frac{1}{Ð_{H_2O,M}^{eff}} \quad \text{and} \tag{87}$$

$$L_6 = -\frac{x_{H_2O}}{Ð_{H_2O,CH_3OH}^{eff}}. \tag{88}$$

The electric potential gradient $\partial\phi^M/\partial z$ in the membrane material, due to the transport resistance to the proton flux ("Ohmic drop" over membrane) is obtained from the Maxwell–Stefan equation for the protons as:

$$\frac{\partial\phi^M}{\partial z} = -\frac{RT^M}{c_{H^+}^M F}(L_{H^+} + n_{H^+}L_7 + n_{H_2O}L_8 + n_{CH_3OH}L_9) \tag{89}$$

with

$$L_{H^+} = -\frac{c_{H^+}^M}{a_{H^+}^M}\frac{\partial a_{H^+}^M}{\partial z}, \tag{90}$$

$$L_7 = \frac{x_{H_2O}}{Ð_{H^+,H_2O}^{eff}} + \frac{x_{CH_3OH}}{Ð_{H^+,CH_3OH}^{eff}} + \frac{1}{Ð_{H^+,M}^{eff}}, \tag{91}$$

$$L_8 = -\frac{x_{H^+}}{Ð_{H^+,H_2O}^{eff}} \quad \text{and} \tag{92}$$

$$L_9 = -\frac{x_{H^+}}{Ð_{H^+,CH_3OH}^{eff}}. \tag{93}$$

The problem with Eq. (89) is, that for the protons no Flory–Huggins non-ideality parameters are known. Therefore, in the above equations, the activity of protons is approximated by the mole fraction of protons in the pore liquid, $x_{H^+}^M$.

For the energy balance in (M), transport equations are needed for thermal conduction and convective heat transport. Both are similar to the equations for (AD) and (CD):

$$\text{Conductive heat flux : } q^M = -\lambda^{M,eff}\frac{\partial T^M}{\partial z}, \tag{94}$$

$$\text{Enthalpy flux (convective heat flux) : } e^M = \sum_j n_j^M h_j(T^M). \tag{95}$$

4. Simulation results

The presented DMFC model was implemented in MatLab using the solver ode15s to carry out dynamic simulations into steady state at a variety of operating conditions. The parameters which were varied are the anode feed temperature T^{AF} and the cell current density i_{cell}. Fig. 4 presents some of the results of these steady state simulations and corresponding experimental data for anode feed temperatures from 30 up to 90 °C at varying cell current densities. All other operating conditions are given in the figure. It has to be emphasised that all simulation results are obtained using the same set of parameters (presented in the preceding sections and the respective appendices). The parameters for the calculation of the binary diffusion coefficients are based on those found in the literature [23], but have been slightly adjusted in order to get a better fit of the experimental data (values given in Table 2). The activation energies used (right column in Table 2) are in the typical range for diffusive transport. Interesting is the high value for the pair water/membrane. Here possibly additional thermal effects are reflected, like those related with solvation.

As one can see from Fig. 4, in general a reasonable approximation to the experimental steady state results has been achieved. The simulation results for the membrane crossover flux densities as well as for the current–voltage curves are in the orders of the experimental data. Also the trends are predicted correctly, i.e. water crossover fluxes increase with current density and methanol crossover fluxes decrease with current density. Especially for the methanol crossover, all simulation results are within or close to the error bars of the experimental data (error bars based on evaluation of the accuracy of the sensors used to determine the crossover fluxes [15]). As the methanol crossover plays a key role for the performance of the DMFC, its correct prediction is one of
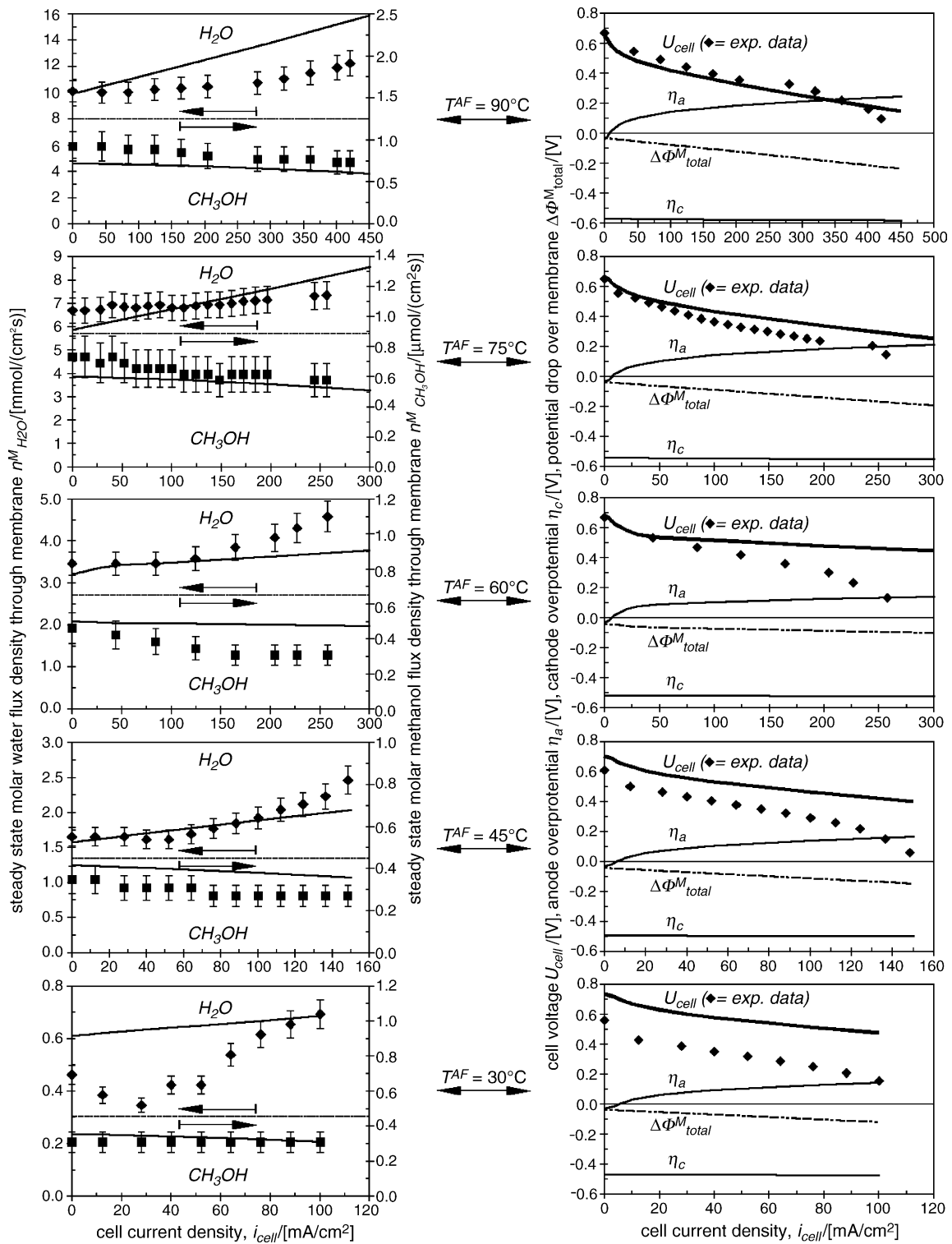
Fig. 4. Experimental (symbols) and simulated results (lines) for a single-cell DMFC. Left: crossover flux densities (left y-axis: H_2O, right y-axis: CH_3OH); right: current–voltage-curves ($T^{AF} = 30, \ldots, 90\,°C$, $p^A = p^C = 1.7\,\text{bar}$, $c^{AF}_{CH_3OH} = 1\,\text{mol}\,\text{dm}^{-3}$, $c^{AF}_{CO_2} = 1\,\mu\text{mol}\,\text{dm}^{-3}$, $F^{AF} = 0.5\,\text{dm}^3\,\text{min}^{-1}$, $F^{CF} = 0.5\,\text{scbm}\,\text{h}^{-1}$, cathode feed: air with dew point $3\,°C$ at $1\,\text{bar}$).

the most important benchmarks of any mathematical DMFC process model.

Significant deviations from the experimental observations exist for the crossover water flux densities at very low and

very high temperatures. The experimental crossover water fluxes through the membrane show an increasing gradient with increasing current density. Such a behaviour can not be explained by the Maxwell–Stefan model, as the model

allows an utmost only linear dependency between flux and current density. Also the binary diffusion coefficients within the membrane material are formulated such, that they are increasing linearly with the local relative water content (a very recent publication supports this assumption [24]). Further optimisation of the parameters for the calculation of the binary diffusion coefficients can be expected to yield even better approximations to the experimental crossover fluxes. For this purpose, numerical optimisation methods can be applied. But for this task, first the computational time of the model should be reduced by either optimising the source code, or implementing the model in other, faster solver tools than MatLab. Finally, also the applied Flory–Huggins activity model influences the simulation results in terms of the membrane crossover fluxes. The Flory–Huggins model was originally formulated for mixtures of uncharged polymers and uncharged solvents, therefore its application to a polymer electrolyte demands further discussion.

After analysing the simulated crossover fluxes, now the simulated current–voltage curves, overpotentials and potentials drops over the membrane are discussed. The results are presented in the left column of Fig. 4. Generally it can be observed that the cathode overpotentials are very high, even for open circuit conditions. This is due to the oxidation of crossover methanol at the cathode, and the resulting mixed potential formation. The influence of the cell current density on the cathode overpotential is only small. In contrast to this, the anode overpotential varies significantly with the cell current density. At open circuit conditions, the anode overpotential is close to zero, for high current densities, values around 0.25 V are found. Finally, the total potential drop over the membrane shows a nearly linear increase with only a small slope. What seems remarkable is the fact, that it is not zero at open circuit conditions. This can be explained with the diffusive flux of water through the membrane, which also takes place when there is no electrical current flow. The water molecules exert a drag on the protons in the membrane, but the protons are withheld by electrostatic forces between them and their counter-ions bound to the membrane material. An electric field is produced by this phenomenon, which is often referred to as streaming potential.

Another observation from Fig. 4 is, that the experimental open circuit cell voltages increase with the cell temperature, while the model predicts a decrease. This is to a large extent due to the fact, that in the model the open circuit cell voltage is calculated from thermodynamics using some simplifying assumptions [15]. These thermodynamic relations exhibit a decrease of the open circuit cell voltage with increasing temperature. The difference between the thermodynamic and the real behaviour results from the fact, that in reality not a one-step total methanol oxidation takes place at the anode (as is assumed in the thermodynamic considerations), but a very complex, multi-step network of adsorption and desorption processes and reaction intermediates exists. A better prediction of the open circuit voltage, based on a more realistic

situation at both electrodes, would significantly enhance the prediction of the current–voltage curves.

Nonetheless, for moderate cell current densities, the model predicts slopes of the current–voltage curves, which are close to the experimental results. In this regime, the cell behaviour is dominated by mass transfer phenomena within the membrane, which seems to be reasonably represented by the model.

At high cell current densities, finally, the predicted cell voltages are much higher than the observed experimental values. Also, the experimental results show a typical limiting current behaviour (breakdown of the cell voltage), while the model shows such limiting current behaviour only for significantly higher cell current densities (not shown in the plots in Fig. 4). Here it becomes evident that the model is based on severe simplifications with respect to mass transport in both diffusion layers. The model does not account for the possible coexistence of two phases (gas and liquid) within both diffusion and catalyst layers, although it is well-known from various experimental observations. Carbon dioxide bubbles are released from the anode diffusion layer [25,26], condensation of water can occur inside the cathode pore structure (so-called cathode flooding) [8]. Both phenomena lead to increased transport resistances for the fuel (methanol) and oxidant (oxygen) to the respective electrodes and they are both most important for high current densities, i.e. for the limiting current behaviour. Such two-phase transport behaviour has therefore to be included in a DMFC model if a realistic simulation of the limiting current behaviour is to be achieved.

As the model is one-dimensional perpendicular to the cell plane, profiles through the DMFC are obtained for concentrations, temperature, pressure and all presented fluxes. Exemplarily selected steady state profiles are presented in Fig. 5 for an anode feed temperature of 60 °C and a cell current density of 200 mA cm^{-2}. All other parameters are the same as those given in Fig. 4. In Fig. 5 the ordinates show the real cell geometry with respect to the thicknesses of the different layers of the DMFC. The vertical lines represent the limits of the control volumes, illustrating the spatial discretisation of both diffusion layers (AD, CD) and the membrane (M). One can see that both diffusion layers are represented by five control volumes each, and that the membrane is discretised into ten control volumes. It is also apparent that the thicknesses (i.e. the volumes) of the diffusion layer control volumes are constant, as these layers consist of a rigid solid matrix. In contrast to this, the thicknesses (and therefore also the total volumes) of the membrane control volumes change due to different water and methanol contents, representing the swelling behaviour of the membrane material. Simplifyingly, in the model all volume changes due to swelling only influence the thicknesses of the control volumes along the model coordinate perpendicular to the cell plane. It has to be mentioned that the thicknesses of the anode and cathode channels, (A) and (C), respectively, do not represent their real dimensions.

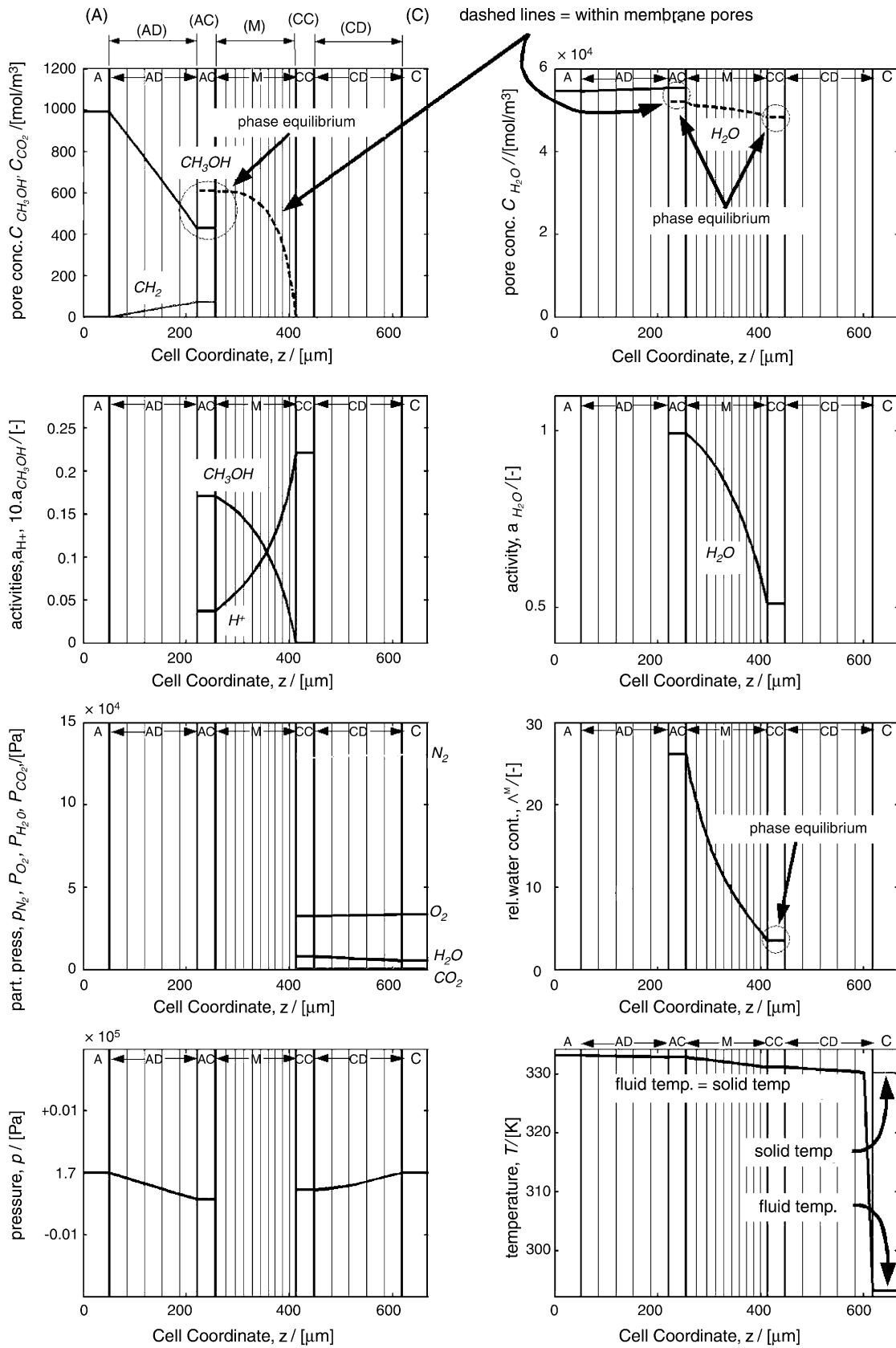One can see that for the diffusion layers,(AD) and (CD), nearly linear concentration and partial pressure profiles are

Fig. 5. Simulated steady state profiles ($T^{AF} = 60\,^{\circ}C$, $i_{cell} = 200\,mA\,cm^{-2}$, all other operating conditions as in Fig. 4). Ordinate represents real cell geometry, vertical lines are limits of control volumes (abbreviations A, AD, etc. used to denote the DMFC layers, see list of symbols).

obtained. The slopes of the partial pressure profiles in (CD) are only small. Also the total pressure differences between the supply channels and the respective catalyst layers are only in the order of a few mPa. Obviously, according to the here applied model, mass transport in the diffusion layers is quite fast, especially on the cathode (i.e. gas) side (as was already pointed out above referring to the limiting current behaviour).

Shown in Fig. 5 are also the phase equilibria for water and methanol within the catalyst layers between the free pore concentrations and the equilibrium concentrations within the membrane material (as described in chapter 3). One can see that on the anode side the methanol concentration in the membrane pores is slightly higher than that in the free pores, while the water concentration in the membrane pores is a little lower than that in the free pores (see circles in the upper two plots of Fig. 5). The phase equilibrium for water in the cathode catalyst layer (CC) is also highlighted by circles in the respective plots.

The most interesting concentration profiles develop within the membrane (dashed concentration profiles in the upper two diagrams of Fig. 5). The methanol pore concentration shows a strongly bent profile in the direction of the overall flow, i.e. towards the cathode. This makes sense as methanol is dragged along with the water flow (diffusion and electro-osmosis). Also the water profile is slightly bent in the same manner due to electro-osmotic transport. Nonetheless, diffusion remains the major mode of transport for methanol and water. Most interesting is the big difference in the water content between anode and cathode side of the membrane. While on the anode side a relative water content of around 26 is reached, on the cathode side only values around 4 are found. This is due to the operation of the cell with dry air at high flow rates. Water is transported away from the cathode catalyst layer (CC) very efficiently, drying out this side of the membrane according to the phase equilibrium relation (Eq. (49)). This change in water content is also illustrated by the decreasing

thickness of the membrane control volumes from anode to cathode.

The conductivity of the membrane is given by the friction exerted on the moving protons. This friction is represented by the binary diffusion coefficients, which in turn are functions of the local water content. Therefore, also the proton conductivity is a function of the local water content and thus varies locally. The same is true for the potential gradient in the membrane.

Finally, the temperature profile exhibits only very small gradients over the inner layers of the DMFC. The total temperature difference between anode channels and outer side of the cathode diffusion layer (CD) is less than 3 K. Only the air in the cathode channels has a much lower temperature close to its inlet temperature, due to the short residence time and the small heat exchange coefficients between channel walls and gas (see discussion in Section 3.9).

From the simulation results, it is possible to evaluate the importance of the different mass transport contributions (driving forces and friction) in the generalised Maxwell–Stefan framework, Eq. (1). Table 3 presents the quintessence of this evaluation. In the top line, the complete Eq. (1) is given. In the following rows the importance of the individual terms of the generalised Maxwell–Stefan equation is indicated for each of the three mass transport related layers of the DMFC and each mobile species by "++" (very important), "+" (moderately important) and blanks (not important/negligible).

Obviously, multi-component diffusion represented by the gradient in the chemical potentials as driving force, left term, and both friction terms (species-species and species–matrix), right side of Eq. (1), are the most important influencing factors for mass transport of all mobile species.

The pressure-dependence of the chemical potentials (second driving force term on the left hand side of Eq. (1)) is negligible in all DMFC layers. This is generally justified for liquid phases if no large pressure gradients exist. This

Table 3
Importance of mass transport contributions in Eq. (1) (driving forces and friction terms): ++ = very important, + = important, blanks= not important/negligible

	$-\dfrac{c_j}{RT}\nabla_{T,p}\mu_j$	$-\dfrac{c_j}{RT}\bar{V}_j\nabla p$	$-\dfrac{\alpha'_j}{Đ_{jM}}c_j\dfrac{B_0}{\eta}\nabla p$	$-c_j z_j^*\dfrac{F}{RT}\nabla\phi$	$=\displaystyle\sum_{i\neq j}\dfrac{x_i n_j - x_j n_i}{Đ_{ij}^{eff}}$	$+\dfrac{n_j}{Đ_{jM}^{eff}}$
AD						
H_2O	++		++		++	+
CH_3OH	++		+		++	+
CO_2	++		+		++	+
M						
H^+	++			++	++	++
H_2O	++				++	++
CH_3OH	++				++	+
CD						
N_2	++		++		++	+
O_2	++		+		++	+
H_2O	++		+		++	+
CO_2	++		+		++	+

term is only relevant for applications with extremely high pressure differences as they can be found e.g. in reverse osmosis and pervaporation processes. On the gas side of the presented model, i.e. in the cathode diffusion layer (CD), it is also negligible due to the very low pressure gradient.

The third driving force is pressure-driven convection. This is accounted for in both diffusion layers and has shown to play an important role especially for the excess components in the respective fluid mixtures, i.e. water in (AD) and nitrogen in (CD). Within the polymer electrolyte membrane this term is neglected due to the low hydraulic permeability.

Finally, the electric field as driving force only applies to protons as the only mobile charged species.

5. Conclusions

Based on a systematic approach, a one-dimensional process model of a DMFC has been developed. In this model, mass transport within the different porous structures of the DMFC is described using the generalised Maxwell–Stefan equations. For the membrane an activity model based on the Flory–Huggins approach is used accounting for swelling phenomena, related non-idealities and phase equilibria at the boundary between membrane material and catalyst layer pores. The model yields good approximations to experimental data with respect to mass transport (crossover) and also reasonable results with respect to steady-state current voltage characteristics. It has to be pointed out, that all simulations were carried out with one single set of parameters.

The most significant deviations between simulated and experimental crossover fluxes occur for high current densities, in the limiting current regime. To get more realistic simulation results in this respect, two-phase flow in the anode (carbon dioxide bubble formation) and cathode (condensation of water = cathode flooding) pore structures has to be accounted for in an improved model.

Also significant deviations exist for the current–voltage characteristics. This can be attributed to the use of simple Butler–Volmer rate equations for both electrode reactions. As the real reaction mechanisms are known to be complex reaction networks with several intermediates, side and parallel reactions and coupled adsorption/desorption phenomena, a Butler–Volmer approach means a significant simplification, and thus can lead to less realistic simulation results, especially in the kinetically dominated region of the current–voltage curves (i.e. for low current densities) (see Tables 4–11).

Summing up, further model refinement and analysis will address the following issues:

- Coexistence of two phases (gas and liquid) in the anode and the cathode diffusion and catalyst layers.

- Influence of pressure differences between anode and cathode on the water and methanol transport through the membrane: can the respective term for pressure-driven convection in the Maxwell–Stefan equations really be neglected? Several experimental studies (also own, yet unpublished, results) have shown an increase in cell performance when on the cathode side of a DMFC a higher pressure is applied than on the anode side. Is this due to decreased methanol crossover, or due to the higher oxygen partial pressure at the cathode?
- Is osmotic pressure (which has not been discussed in this paper at all) intrinsically accounted for using the Flory–Huggins activity model?
- More realistic models for the anode and cathode reaction kinetics accounting for reaction intermediates, adsorption/desorption phenomena etc.

Appendix A. Physical properties of pure substances

A.1. Densities

The densities of all liquid and solid materials are assumed to be independent of temperature and pressure. They are collected in Table 4. All gases are assumed to be ideal, therefore the density of dry air can be calculated using the ideal gas law:

$$\rho_{air}(p, T) = \frac{M_{air}}{V_{air}} = \frac{p}{R_{air}T} \quad (A.1)$$

with the specific gas constant of air $R_{air} = 287.22 \, \text{J kg}^{-1} \, \text{K}^{-1}$ [31], temperature T in (K) and pressure p in (Pa).

The density of the mixed anode catalyst can be calculated from the mass fractions w of both metals and their densities:

$$\rho_{PtRu} = w_{Pt}\rho_{Pt} + w_{Ru}\rho_{Ru} = 0.66 \cdot 21400 + 0.34 \cdot 12400$$
$$= 18300 \, \text{kg m}^{-3} \quad (A.2)$$

A.2. Heat capacities

Literature data for pure substances are given in Table 5. For air as a standard mixture of mainly nitrogen and oxygen,

Table 4
Mass densities

Component j	Density ρ_j (kg m^{-3})
Liquid water, H_2O (l)	997 [27d]
Liquid methanol, CH_3OH (l)	791 [27d]
Carbon/graphite (base material of TORAY™ carbon paper)	2000
Teflon™, PTFE	2190 [28]
Dry Nafion™	1970 [30]
Platinum, Pt	21400 [29]
Ruthenium, Ru	12400 [29]

Table 5
Heat capacities

Component j	Heat capacity	
	$\bar{C}_{p,j}$ (J mol^{-1} K^{-1})	$C_{p,j}$ (J kg^{-1} K^{-1})
Liquid water, H$_2$O (l) [27b]	75.29 [27b]	4183 [27b]
Carbon/graphite (material of TORAY™ carbon paper)	8.23 [32]	685 [32]
Teflon™, PTFE	–	1010 [28]
Platinum, Pt	–	130 [29]
Ruthenium, Ru	–	238 [29]
Oxygen, O$_2$(g)	29.36 [27b]	–
Nitrogen, N$_2$(g)	29.13 [27b]	–
Water vapour, H$_2$O(g)	33.58 [27b]	–
Carbon dioxide gas, CO$_2$(g)	37.11 [27b]	–

a mean heat capacity can be assumed:

$$\bar{C}_{p,\text{air}} = 0.79 \cdot \bar{C}_{p,\text{N}_2} + 0.21 \cdot \bar{C}_{p,\text{O}_2} = 29.18 \,\text{J mol}^{-1}\,\text{K}^{-1}. \tag{A.3}$$

The mass-based value can be obtained by accounting for the molar masses of oxygen and nitrogen:

$$C_{p,\text{air}} = 0.79 \cdot \frac{\bar{C}_{p,\text{N}_2}}{\bar{M}_{\text{N}_2}} + 0.21 \cdot \frac{\bar{C}_{p,\text{O}_2}}{\bar{M}_{\text{O}_2}} = 1015 \,\text{J kg}^{-1}\,\text{K}^{-1}. \tag{A.4}$$

A.3. Thermal conductivities

For liquid water and air data for different temperatures are given in the literature (e.g. for water: [33a], for air: [33b]). The thermal conductivity is showing a nearly linear increase with temperature. Linear regressions yield the following simple expressions (with temperature T in (K) and λ_j in (W m^{-1} K^{-1})):

$$\lambda_{\text{H}_2\text{O}(l)} = 0.341 + 9.26 \times 10^{-4} \cdot T \tag{A.5}$$

$$\lambda_{\text{air}} = 0.0034 + 7.6 \times 10^{-5} \cdot T \tag{A.6}$$

For wet Nafion™, in the literature a value of

$$\lambda_{\text{wet Nafion}} = 0.43 \,\text{W m}^{-1}\text{K}^{-1} \tag{A.7}$$

is reported [23].

A.4. Specific enthalpies

The specific enthalpies h_j (J mol^{-1} K^{-1}) of the fluid components are calculated from the standard enthalpies

Table 6
Standard enthalpies of formation [27b]

Component j	$\Delta_{\text{R}} H_j^\theta$ (kJ mol^{-1})
Liquid water, H$_2$O (l)	−285.83
Oxygen, O$_2$(g)	0
Nitrogen, N^2(g)	0
Water vapour, H$_2$O (g)	−241.82
Carbon dioxide gas, CO$_2$ (g)	−393.51

of formation, $\Delta_{\text{F}} H_j^\theta$ (J mol^{-1} K^{-1}) at standard temperature $T^\theta = 298.15$ K, and the specific heat capacities $\bar{C}_{p,j}$ (J mol^{-1} K^{-1}):

$$h_j = \Delta_{\text{F}} H_j^\theta + \bar{C}_{p,j}(T - T^\theta). \tag{A.8}$$

The values for the heat capacities are given in Section A.2. The standard enthalpies of formation are presented in Table 6.

For liquid methanol, no standard enthalpy of formation was found, but absolute values of the specific enthalpy for different temperatures [33c]. A linear regression and conversion from mass to molar basis yields the expression

$$h_{\text{CH}_3\text{OH}(l)} = -3726 + 48.8T \tag{A.9}$$

with $h_{\text{CH}_3\text{OH}(l)}$ in (J mol^{-1}) and T in (K).

A.5. Viscosities

According to [34a] the viscosity of pure liquids in (Pa s) can be calculated from expressions of the type

$$\eta_j^{\text{vis}} = 10^{-3} \exp\left(A_j + \frac{B_j}{T} + C_j T + D_j T^2 \right) \tag{A.10}$$

with temperature T in (K). Table 7 presents the values of the parameters for water, methanol and carbon dioxide as well as the temperature range, for which they are valid.

At pressures well below 10 bars (10^6 Pa), the viscosity of most gases and gas mixtures is nearly independent of the pressure, but only a function of temperature. For air values for different temperatures (at a pressure of 1 bars = 10^5 Pa) are available in the literature. These data show a nearly linear dependence between viscosity and temperature. A linear regression yields the expression

$$\eta_{\text{air}}^{\text{vis}} = (4.65 + 0.0464 \cdot T) \cdot 10^{-6} \tag{A.11}$$

where the temperature T is in (K) and the viscosity results in (Pa s). The relative error compared to the literature values is below 0.4%.

Table 7
Parameters for calculation of liquid viscosities [34a]

Component j	T (°C)	A_j	B_j	C_j	D_j
Water, H$_2$O(l)	0 to +370	−24.700	4209	0.04527	−3.376 × 10^{-5}
Methanol, CH$_3$OH(l)	−40 to +239	−39.350	4826	0.10910	−1.127 × 10^{-4}
Carbon dioxide, CO$_2$(l)	−56 to +30	−3.097	48.86	0.02381	−7.840 × 10^{-5}

Table 8
Antoine equation parameters for calculation of vapour pressures [32]

Temperature range	A_j	B_j	C_j
Water, H_2O			
304–333 K	5.20389	1733.926	−39.485
334–363 K	5.07680	1659.793	−45.854
Methanol, CH_3OH			
288–356.83 K	5.20409	1581.341	−33.500
353.4–512.63 K	5.15853	1569.613	−34.846

A.6. Vapour pressures

The vapour pressures of water and methanol can be calculated using the Antoine equation [32]

$$\log_{10}\left(p_{\mathrm{sat},j}(\mathrm{bar})\right) = A_j - \frac{B_j}{(T(\mathrm{K})) + C_j} \qquad (\mathrm{A}.12)$$

The parameters A_j, B_j, C_j are given in Table 8.

A.7. Liquid molar volumes

For water and methanol, literature values are available [34b]:

$$\bar{V}_{H_2O} = 18.7 \times 10^{-6}\,\mathrm{m^3\,mol^{-1}} \qquad (\mathrm{A}.13)$$

$$\bar{V}_{CH_3OH} = 42.5 \times 10^{-6}\,\mathrm{m^3\,mol^{-1}}. \qquad (\mathrm{A}.14)$$

The value for carbon dioxide can be calculated using the method of Schroeder [34c] as

$$\bar{V}_{CO_2} = (3+2) \cdot 7\,\mathrm{cm^3\,mol^{-1}} = 35 \times 10^{-6}\,\mathrm{m^3\,mol^{-1}}. \qquad (\mathrm{A}.15)$$

Applying the same method, a proton has a molar volume of

$$\bar{V}_{H^+} = 7 \times 10^{-6}\,\mathrm{m^3\,mol^{-1}}. \qquad (\mathrm{A}.16)$$

A.8. Speed of sound

For ideal gases the speed of sound is related to the ratio of the specific heat capacities $\kappa = C_p/C_v$, the temperature T in (K), the molar mass $\bar{M}_j$ in (kg/mol) and the universal gas constant $R = 8.314\,\mathrm{J/(mol\,K)}$ [33e]:

$$\kappa_{\mathrm{sound},j} = \sqrt{\frac{k_j R T}{\bar{M}_j}}. \qquad (\mathrm{A}.17)$$

For air, the heat capacity ratio in the important temperature range (300, ..., 400 K) and pressure range (1.5×10^5 Pa) is nearly constant at a value of 1.4 [33f].

The molar mass of air can be approximated assuming air consisting only of oxygen and nitrogen with the respective mole fractions $y_{O_2} = 0.21$ and $Y_{N_2} = 0.79$:

$$\bar{M}_{\mathrm{air}} \approx y_{O_2}\bar{M}_{O_2} + y_{N_2}\bar{M}_{N_2} = 28.84\,\mathrm{g\,mol^{-1}}. \qquad (\mathrm{A}.18)$$

The speed of sound in water in the respective temperature and pressure range is nearly constant at a value of $v_{\mathrm{sound},H_2O} = 1500\,\mathrm{m\,s^{-1}}$.

A.9. Diffusion coefficients

Two types of binary diffusion coefficients are necessary for the modeling of mass transfer using the Maxwell–Stefan approach: One for each pair of the mobile species and one for each mobile species' interaction with the wall of the porous structure. In general, all binary diffusion coefficients depend on the temperature and the overall composition.

A.9.1. Diffusion coefficients in the polymer electrolyte membrane (M)

For Nafion™, extensive studies have been made to determine those diffusion coefficients from experimental data. In [23] such expressions are presented. But as most research in polymer electrolyte membrane fuel cells is focused on hydrogen-consuming cells, these expressions are not accounting for methanol but just water within the ionomer pores. The expressions are of an Arrhenius type to account for the temperature influence. As only composition influence, the relative water content Λ^M as ratio between water and sulfonic acid groups' mole fraction is accounted for. As the sulfonic acid groups at the pore walls are not balanced, it is more convenient to use the proton mole fraction instead (electroneutrality). The general expression for the binary diffusion coefficients in ($\mathrm{m^2\,s^{-1}}$) according to [23] is:

$$Đ_{ij}^{\mathrm{eff}}(T, \Lambda^M) = Đ_{ij}^{\theta}\Lambda^M \exp\left[-\frac{E_{ij}^A}{R}\left(\frac{1}{T} - \frac{1}{T^{\theta}}\right)\right] \qquad (\mathrm{A}.19)$$

with the reference temperature $T^{\theta} = 298$ K. The values of the standard diffusion coefficients and the activation energies are given in Table 2.

As in the case of the DMFC also methanol is present within the membrane pores, three more binary diffusion coefficients are necessary for the pairs (CH_3OH/H_2O), (CH_3OH/H^+) and (CH_3OH/M). As for the latter two no literature data are available, they have to be estimated and fitted. As the methanol concentration is very low compared to that of water, an error in these two diffusion coefficients should have only a weak influence on the diffusion of water and protons. But the diffusion of methanol is of course severely depending on these three values. Nonetheless, as methanol is in many respects not so different from water (highly polar, small compact molecule) as a first approach it is assumed that methanol has the same diffusion properties as water, consequently the same parameters are used as starting point for the fitting procedure. They are shown in Table 2.

The remaining binary diffusion coefficient for the pair (H_2O/CH_3OH) is calculated assuming a free solution of methanol in water at infinite dilution (correlation of Hayduk and Minhas for solutes in aqueous solutions [34d], diffusion

coefficient in $(m^2\,s^{-1})$):

$$\text{Đ}_{CH_3OH,H_2O} \approx D^{\infty}_{CH_3OH,H_2O}$$

$$= 1.25 \times 10^{-12}(\bar{V}^{-0.19}_{CH_3OH} - 0.292)T^{1.52}(\eta^{vis}_{H_2O})^{\epsilon*} \quad (A.20)$$

with the exponent

$$\epsilon^* = \frac{9.58}{\bar{V}_{CH_3OH}} - 1.12, \quad (A.21)$$

the molar volume of methanol $\bar{V}_{CH_3OH} = 42.5\,cm^3\,mol^{-1}$ and the viscosity of pure water $\eta^{vis}_{H_2O}$ in $(cP = 10^3\,Pa\,s)$.

A.9.2. Diffusion coefficients in the anode diffusion layer (AD)

The binary diffusion coefficients of the mobile species in the anode diffusion layer (AD) are calculated using the Tyn-Calus method [34e]for diffusion coefficients in liquid solutions at infinite dilution (in $(m^2\,s^{-1})$):

$$D^{\infty}_{ij} = 8.93 \times 10^{-12} \left(\frac{\bar{V}_i}{\bar{V}_j^2}\right)^{1/6} \left(\frac{P_j}{P_i}\right)^{0.6} \frac{T}{\eta^{vis}_j}. \quad (A.22)$$

Here component i is the solute and j is the solvent. The molar volumes $\bar{V}_j$ are in $(cm^3\,mol^{-1})$, the viscosities η^{vis}_j in $(cP = 10^3\,Pa\,s)$ and the temperature T in (K). P_i and P_j are so-called parachors, which are related to the liquid surface tension, but can also be estimated from a groups contribution method developed by Quayle [34e]. For water, methanol and carbon dioxide, this method leads to parachor values of

$$P_{H_2O} = 2 \cdot P_H + P_{-O-} = 2 \times 15.5 + 20$$
$$= 51\,cm^3\,g^{0.25}\,s^{-0.5}, \quad (A.23)$$

$$P_{CH_3OH} = P_{CH_3} + P_{-OH} = 55.5 + 29.8$$
$$= 85.3\,cm^3\,g^{0.25}\,s^{-0.5}, \quad (A.24)$$

$$P_{CO_2} = P_C + 2 \cdot P_O = 9 + 2 \times 20 = 49\,cm^3\,g^{0.25}\,s^{-0.5}. \quad (A.25)$$

According to the literature, if water is the solute, the parachor and molar volume values of water shall be doubled (water is treated as a dimer).

With the help of Eq. (A.22), all six diffusion coefficients at infinite dilution for the three species (water, methanol, carbon dioxide) can be calculated. To get the necessary three binary diffusion coefficients, each pair of the former six values belonging to the same two species are combined using the method of Vignes [34f]:

$$\text{Đ}_{ij} \approx D_{ij} = \alpha_{Vignes}[(D^{\infty}_{ij})^{x_j}(D^{\infty}_{ji})^{x_i}]. \quad (A.26)$$

Both mole fractions x_i and x_j are set to 0.5, the thermodynamic factor α_{Vignes} is assumed to be 1 (ideal mixing behaviour of the two species), leaving the expression

$$\text{Đ}_{ij} = (D^{\infty}_{ij} D^{\infty}_{ji})^{0.5}. \quad (A.27)$$

As the mass transport takes place within a porous matrix, effective diffusion coefficients are needed. To convert the gained values into effective coefficients, it has to be accounted for the morphology of the solid matrix represented by the porosity ε and the tortuosity coefficient τ [18]. (Note that there is a mistake in the mentioned reference: there both diffusion coefficient's indices have been confused.)

$$\text{Đ}^{eff}_{ij} = \frac{\varepsilon}{\tau}\text{Đ}_{ij}. \quad (A.28)$$

To describe the ratio between tortuosity coefficient and porosity, many approximations exist. According to [18],one of the most commonly used is based on the approximation that the tortuosity is only a function of the porosity (and not of the size of the mobile species):

$$\tau = \varepsilon^{-1.5}. \quad (A.29)$$

A.9.3. Diffusion coefficients in the cathode diffusion layer (CD)

In the cathode diffusion layer it is assumed that all mobile species (oxygen, nitrogen, water vapour and carbon dioxide) are ideal gases. The diffusion coefficients describing the influence of the pore wall are calculated using the Knudsen equation (according to [18]),

$$\text{Đ}^{eff}_{jM} = \frac{\varepsilon}{\tau}\frac{d_{pore}}{3}\sqrt{\frac{8RT}{\pi\bar{M}_j}}, \quad (A.30)$$

although here, strictly speaking, no Knudsen diffusion takes place due to the big mean pore diameter in the carbon paper which is some orders of magnitude bigger than the gas molecule diameters. It turns out that the coefficients calculated from Eq. (A.30) are of such an order of magnitude, that in the end there is no significant influence of the wall friction on diffusion.

The pair diffusion coefficients of the mobile species are calculated according to the method of Fuller, Schettler and Giddings in free gas phase [33d](in $(m^2\,s^{-1})$):

$$\text{Đ}_{ij} \approx D_{ij} = \frac{10^{-7}T^{1.75}\sqrt{(\bar{M}_i + \bar{M}_j)/\bar{M}_i\bar{M}_j}}{p[(\sum \bar{V}^*)^{1/3}_i + (\sum \bar{V}^*)^{1/3}_j]^2}. \quad (A.31)$$

Here the temperature T is in (K), $\bar{M}$ are the molecular weights in (g/mol), p is the pressure in $(atm = 10^5\,Pa)$ and the sum terms are sums of atomic diffusion volumes, which are tabulated for many simple gases (Table 9). To get effective diffusion coefficients, also here Eq. (A.28) is used.

In the simulations, the presented diffusion coefficients were used as starting values. In order to get a better fit to experimental data, some of these values have been slightly adjusted, as presented in Table 2.

Table 9
Parameter values for Eq. (A.31) (atomic diffusion volumes taken from [33d])

	O_2	N_2	H_2O	CO_2
M_j (g mol^{-1})	32	28	18	44
$(\sum \bar{V}^*)_j$ (cm^3 mol^{-1})	16.6	17.9	12.7	26.9

Table 10
Physical properties of TGP-H-060 carbon paper [35]

Thickness (μm)	Electrical resistivity (mΩ cm)		Thermal conductivity (W m^{-1} K^{-1})			Porosity (–)	Bulk density (g cm^{-3})
	Through plane	In plane	Through plane (20 °C)	In plane (20 °C)	in plane (100 °C)		
190 (170)[a]	80	5.8	1.7	21	23	0.78	0.44

[a] Own measurement used for further calculations.

Appendix B. Porosities and volume fractions

The major physical properties of TORAY™ paper TGP-H-060 (according to data sheet supplied by Toray Deutschland GmbH) are given in Table 10. As the carbon paper is PTFE treated prior to use in the DMFC, the real porosity has to be calculated as a function of the PTFE content. The total volume of the carbon paper is the sum of the carbon, the PTFE and the free pore volume:

$$V_{tot} = V_{carbon} + V_{PTFE} + V_{pores} \qquad (B.1)$$

The carbon volume can be expressed by the porosity of the untreated carbon paper (see Table 10):

$$V_{carbon} = (1 - \varepsilon_{pores}^{untreated\,Toray})V_{tot} \qquad (B.2)$$

The carbon volume fraction is consequently

$$\varepsilon_{carbon}^{untreated\,Toray} = \varepsilon_{carbon}^{PTFE-treated\,Toray}$$
$$= 1 - \varepsilon_{pores}^{untreated\,Toray} = 0.22. \qquad (B.3)$$

The PTFE mass fraction

$$w_{PTFE} = \frac{m_{PTFE}}{m_{carbon} + m_{PTFE}} \qquad (B.4)$$

can be rearranged to get the PTFE mass

$$m_{PTFE} = \frac{w_{PTFE}}{1 - w_{PTFE}} m_{carbon} \qquad (B.5)$$

Substituting masses by bulk densities times volumes and rearranging we get the PTFE volume

$$V_{PTFE} = \frac{w_{PTFE}}{1 - w_{PTFE}} \frac{\rho_{carbon}}{\rho_{PTFE}} V_{carbon}. \qquad (B.6)$$

Substituting the carbon volume using Eq. (B.2) one gets

$$V_{PTFE} = \frac{w_{PTFE}}{1 - w_{PTFE}} \frac{\rho_{carbon}}{\rho_{PTFE}} (1 - \varepsilon_{pores}^{untreated\,Toray})V_{tot}. \qquad (B.7)$$

The resulting porosity (i.e. the pore volume fraction) of the PTFE-treated material is then

$$\varepsilon_{pores}^{PTFE-treated\,Toray}$$
$$= \frac{V_{pores}}{V_{tot}} = \varepsilon_{pores}^{untreated\,Toray}$$
$$- \frac{w_{PTFE}}{1 - w_{PTFE}} \frac{\rho_{carbon}}{\rho_{PTFE}} (1 - \varepsilon_{pores}^{untreated\,Toray}). \qquad (B.8)$$

With the parameters given in Table 11, the typical PTFE mass content $w_{PTFE} = 0.25$ and the bulk densities of carbon and PTFE, $\varrho_{PTFE} = 2.19$ g/cm^3 and $\varrho_{carbon} = 2.0$ g/cm^3 the porosity of the PTFE-treated TORAY™ paper results as

$$\varepsilon_{pores}^{PTFE-treated\,Toray} = 0.71. \qquad (B.9)$$

The PTFE volume fraction is then finally

$$\varepsilon_{PTFE}^{PTFE-treated\,Toray} = 1 - \varepsilon_{pores}^{PTFE-treated\,Toray}$$
$$- \varepsilon_{carbon}^{PTFE-treated\,Toray} = 0.07. \qquad (B.10)$$

Also the porosity of the catalyst layers has to be determined. It can be calculated as the sum of the volumes of all dry materials within the catalyst layer (i.e. catalyst and NAFION™) divided by the total volume of the catalyst layer. The catalyst and NAFION™ volumes are calculated from the masses and the densities:

$$\varepsilon = \frac{\text{total volume} - \text{catalyst volume} - \text{NAFION volume}}{\text{total volume}} \qquad (B.11)$$

One ends up with an equation using the catalyst and NAFION™ loadings w_{cat} and w_{NAFION}, and the catalyst layer thickness $d^{cat.layer}$:

$$\varepsilon = \frac{1/A^S(V_{tot}^{cat.layer} - (m_{cat}/\rho_{cat}) - (m_{NAFION}/\rho_{NAFION}))}{1/A^S(V_{tot}^{cat.layer})}$$
$$= \frac{d^{cat.layer} - (w_{cat}/\rho_{cat}) - (w_{NAFION}/\rho_{NAFION})}{d^{cat.layer}}. \qquad (B.12)$$

Table 11
Physical properties of catalyst layers and calculation of porosities

Property	AC	CC
Thickness ($d^{cat.layer}$)	35 μm	35 μm
Catalyst loading (w_{cat})	5 mg cm^{-2}	5 mg cm^{-2}
Catalyst density (ρ_{cat})	0.66 × 21.4 + 0.34 × 12.4 = 18.3 g cm^{-3} (Pt:Ru mass ratio 66:34)	21.4 g cm^{-3} (Pt)
NAFION™ loading (w_{NAFION})	0.15 w_{cat} = 0.75 mg cm^{-2}	0.10 w_{cat} = 0.5 mg cm^{-2}
NAFION™ density (ρ_{NAFION})	1.97 g cm^{-3}	1.97 g cm^{-3}
Calculation of volume fractions		
Catalyst (solid metal)	0.08	0.07
NAFION™	0.11	0.07
Free pore space = porosity (ε)	0.81	0.86

For the applied MEAs the resulting calculations are shown in Table 11.

Appendix C. Effective thermal conductivities

From Toray Corporation a value for the through-plane thermal conductivity is available (see Table 10). But this value is only valid for the pores being filled with air, at 20 °C. Therefore, this value is not applicable for the anode diffusion layer (AD) where the pores are filled with water (and traces of methanol and carbon dioxide). Also, as the thermal conductivity of air is temperature dependent, using this value for the cathode diffusion layer seems problematic. Therefore, first the thermal conductivity of the carbon fibres alone shall be calculated. Generally, assuming parallel thermal conduction through all present materials, the effective thermal conductivity can be calculated from

$$\lambda^{\text{eff}} = \sum_j \varepsilon_j \lambda_j. \tag{C.1}$$

Using this expression for TORAY™ paper at 20 °C we get the (assumed temperature-independent) thermal conductivity of TORAY™ paper in the vacuum (i.e. the contribution from the carbon material only):

$$\lambda_{\text{Toray}} = \frac{\lambda_{\text{Toray}+\text{air}}^{\text{eff},20^{\circ}\text{C}} - \varepsilon_{\text{pores}}^{\text{untreated Toray}} \lambda_{\text{air}}^{20^{\circ}\text{C}}}{1 - \varepsilon_{\text{pores}}^{\text{untreated Toray}}}$$

$$= 7.63 \, \text{W m}^{-1} \, \text{K}^{-1} \tag{C.2}$$

The thermal conductivity of air at 20 °C is calculated from Eq. (A.6). The other values are taken from Table 11.

Using the value calculated in Eq. (C.2) and the volume fractions of carbon fibres and PTFE as well as the porosity (see Appendix B), the effective thermal conductivity can be calculated accounting for the material filling the pores and for the temperature.

In the anode diffusion layer (AD) the pores are assumed to be filled with a liquid mixture, which mainly consists of water. For simplicity, the influence of methanol and carbon dioxide is neglected. The resulting expression is

$$\lambda^{\text{eff,AD}} = \varepsilon_{\text{carbon}}^{\text{PTFE}-\text{treated Toray}} \lambda_{\text{Toray}} + \varepsilon_{\text{PTFE}}^{\text{PTFE}-\text{treated Toray}} \lambda_{\text{PTFE}}$$

$$+ \varepsilon_{\text{pores}}^{\text{PTFE}-\text{treated Toray}} \lambda_{\text{H}_2\text{O}}(T) \tag{C.3}$$

For the thermal conductivity of water, the literature value Eq. (A.5) is used.

In the cathode diffusion layer (CD) the pores are assumed to be filled with air. Eq. (A.6) is used for the thermal conductivity of air.

$$\lambda^{\text{eff,CD}} = \varepsilon_{\text{carbon}}^{\text{PTFE}-\text{treated Toray}} \lambda_{\text{Toray}} + \varepsilon_{\text{PTFE}}^{\text{PTFE}-\text{treated Toray}} \lambda_{\text{PTFE}}$$

$$+ \varepsilon_{\text{pores}}^{\text{PTFE}-\text{treated Toray}} \lambda_{\text{air}}(T) \tag{C.4}$$

Appendix D. Volumetric effective heat capacities

In the energy balances of the simulation model, the volumetric overall heat capacities in all control volumes are needed. These are calculated from the densities ρ_j (kg m^{-3}), the mass-based heat capacities $C_{p,j}$ (J kg^{-1} K^{-1}) and volume fractions ε_j (–) of all present materials and reactants:

$$(\widetilde{\rho C_p}) = \sum_j \varepsilon_j \rho_j C_{p,j}. \tag{D.1}$$

The pores in the anode diffusion layer (AD) are assumed to be filled with liquid water and small amounts of methanol and carbon dioxide. As the mole fractions of the latter two are each well below 0.05, their influence on the overall heat capacity is neglected. It is only accounted for the carbon material and the PTFE forming the solid porous structure as well as the water inside the pores:

$$(\widetilde{\rho C_p})^{\text{AD}} = \varepsilon_{\text{carbon}}^{\text{PTFE}-\text{treated Toray}} \rho_{\text{carbon}} C_{p,\text{carbon}}$$

$$+ \varepsilon_{\text{PTFE}}^{\text{PTFE}-\text{treated Toray}} \rho_{\text{PTFE}} C_{p,\text{PTFE}}$$

$$+ \varepsilon_{\text{pores}}^{\text{PTFE}-\text{treated Toray}} \rho_{\text{H}_2\text{O(l)}} C_{p,\text{H}_2\text{O(l)}}. \tag{D.2}$$

The identical equation is applied to the cathode diffusion layer (CD). The only difference is that the pores are filled with air instead of liquid water.

As in the anode diffusion layer (AD), all pores in the anode catalyst layer (AC) are assumed to be filled with pure water. Methanol and carbon dioxide are again neglected. Here the solid matrix is formed from the catalyst particles and ionomer (Nafion™):

$$(\widetilde{\rho C_p})^{\text{AC}} = \varepsilon_{\text{PtRu}}^{\text{AC}} (\widetilde{\rho C_p})_{\text{PtRu}} + \varepsilon_{\text{Nafion}}^{\text{AC}} (\widetilde{\rho C_p})_{\text{Nafion}}$$

$$+ \varepsilon_{\text{pores}}^{\text{AC}} \rho_{\text{H}_2\text{O(l)}} C_{p,\text{H}_2\text{O(l)}} \tag{D.3}$$

with the heat capacity of the PtRu catalyst calculated from the mass fractions of both metals:

$$(\widetilde{\rho C_p})_{\text{PtRu}} = 0.66 \rho_{\text{Pt}} C_{p,\text{Pt}} + 0.34 \rho_{\text{Ru}} C_{p,\text{Ru}}$$

$$= 2.84 \times 10^6 \, \text{J m}^{-3}\text{K}^{-1} \tag{D.4}$$

In the literature [23] for wet NAFION™ one finds a volumetric heat capacity of

$$(\widetilde{\rho C_p})_{\text{Nafion}} = 2.4 \times 10^7 \text{J m}^{-3}\text{K}^{-1}. \tag{D.5}$$

For the cathode catalyst layer (CC) the same reasoning is valid as for the anode catalyst layer (AC), except that the pores are filled with air, and the catalyst is pure platinum.

Appendix E. Concentration measures within the PEM

To convert the concentration measures used in the PEM model, the concentration with respect to the total volume

including the polymer backbone $\tilde{c}_i$ (mol m^{-3}) is useful. It can be calculated from the molar density $\hat{N}_{j,k}^M$ in the spatially discretised model as

$$\tilde{c}_{j,k}^M = \frac{\hat{N}_{j,k}^M}{\Delta z_k^M} \tag{E.1}$$

with $j = H_2O$, CH_3OH, H^+, where the thickness Δz_k^M (m) of the respective control volume k is calculated from

$$\Delta z_k^M = \frac{d^{M,dry}}{ncv^M} + \sum_j \left(\hat{N}_{j,k}^M \bar{V}_j \right). \tag{E.2}$$

This thickness is also needed for the various flux calculations to calculate the distances between the centres of the control volumes. From $\tilde{c}_j$, all other concentration measures can be easily calculated:

volume fractions : $\varepsilon_j^M = \tilde{c}_j^M \bar{V}_j$. $\tag{E.3}$

concentrations within the pores : $c_j^M = \dfrac{\tilde{c}_j^M}{\varepsilon_{pores}^M}$, $\tag{E.4}$

with

$$\varepsilon_{pores}^M = \sum_j \varepsilon_j^M = \varepsilon_{H^+}^M + \varepsilon_{H_2O}^M + \varepsilon_{CH_3OH}^M. \tag{E.5}$$

References

[1] K. Sundmacher, T. Schultz, S. Zhou, K. Scott, M. Ginkel, E.D. Gilles, Chem. Eng. Sci. 56 (2) (2001) 333–341.
[2] S. Zhou, T. Schultz, M. Peglow, K. Sundmacher, Phys. Chem. Chem. Phys. 3 (3) (2001) 347–355.
[3] K. Scott, W.M. Taama, J. Cruickshank, J. Power Sources 65 (1997) 159–171.
[4] K. Scott, P. Argyropoulos, K. Sundmacher, J. Electroanal. Chem. 477 (1999) 97–110.
[5] K. Sundmacher, K. Scott, Chem. Eng. Sci. 54 (1999) 2927–2936.
[6] A.A. Kulikovsky, Electrochem. Commun. 5 (2003) 530–538.
[7] K.T. Jeng, C.W. Chen, J. Power Sources 112 (2002) 367–375.
[8] A. Siebke, W. Schnurnberger, F. Meier, G. Eigenberger, Fuel Cells 3 (1) (2003) 1–11.
[9] J.P. Meyers, J. Newman, J. Electrochem. Soc. 149 (6) (2002) A710–A717.
[10] J.P. Meyers, J. Newman, J. Electrochem. Soc. 149 (6) (2002) A718–A728.
[11] J.P. Meyers, J. Newman, J. Electrochem. Soc. 149 (6) (2002) A729–A735.
[12] G. Murgia, L. Pisani, A.K. Shukla, K. Scott, J. Electrochem. Soc. 150 (9) (2003) A1231–A1245.
[13] P. Argyropoulos, K. Scott, A.K. Shukla, C. Jackson, J. Power Sources 123 (2003) 190–199.
[14] H. Guo, C. Ma, Electrochem. Commun. 6 (2004) 306–312.
[15] T. Schultz, Experimental and model-based analysis of the steady-state and dynamic operating behaviour of the direct methanol fuel cell (DMFC), Dissertation thesis, Otto-von-Guericke University Magdeburg, 2004.
[16] L. Jörissen, V. Gogel, J. Kerres, J. Garche, J. Power Sources 105 (2002) 267–273.
[17] J.A. Wesselingh, R. Krishna, Mass Transfer in Multicomponent Mixtures, Delft University Press, Delft, 2000.
[18] R. Krishna, J.A. Wesselingh, Chem. Eng. Sci. 52 (6) (1997) 861–911.
[19] J. Gmehling, J. Li, M. Schiller, Ind. Eng. Chem. Res. 32 (1) (1993) 178–193.
[20] J.A. Wesselingh, P. Vonk, G. Kraaijeveld, Chem. Eng. J. 57 (1995) 75–89.
[21] T.A. Zawodzinski, C. Derouin, S. Radzinski, R.J. Sherman, V.T. Smith, T.E. Springer, S. Gottesfeld, J. Electrochem. Soc. 140 (4) (1993) 1041–1047.
[22] M. Laporta, M. Pegoraro, L. Zanderighi, Phys. Chem. Chem. Phys. 1 (1999) 4619–4628.
[23] M. Wöhr, K. Bolwin, W. Schnurnberger, M. Fischer, W. Neubrand, G. Eigenberger, Int. J. Hydrogen Energy 23 (3) (1997) 213–218.
[24] F. Meier, J. Kerres, G. Eigenberger, J. Membr. Sci. 241 (2004) 137–141.
[25] K. Scott, W.M. Taama, P. Argyropoulos, J. Power Sources 79 (1999) 43–59.
[26] P. Argyropoulos, K. Scott, W.M. Taama, Electrochim. Acta 44 (20) (1999) 3575–3584.
[27] (a) P.W. Atkins, Physikalische Chemie, VCH, Weinheim, 1990, p. 857 (Tab.0–1);
(b) P.W. Atkins, Physikalische Chemie, VCH, Weinheim, 1990, p. 860 (Tab.4–1).
[28] Data sheet for PTFE supplied by Bohlender GmbH, Grünsfeld (Germany).
[29] Data sheets for platinum and ruthenium black catalysts, supplied by Alfa Aesar Johnson Matthey GmbH, Karlsruhe, Germany.
[30] Data sheets for Nafion™, supplied by DuPont.
[31] VDI-Wärmeatlas 9. Auflage, VDI-Verlag, Frankfurt, 2002 (section Dbb1.)
[32] NIST webbook at http://www.webbook.nist.gov.
[33] (a) R.H. Perry, D. Green, Perry's Chemical Engineers' Handbook, sixth ed., McGraw-Hill, New York, 1984, pp. 3–253;
(b) R.H. Perry, D. Green, Perry's Chemical Engineers' Handbook, sixth ed., McGraw-Hill, New York, 1984, pp. 3–254;
(c) R.H. Perry, D. Green, Perry's Chemical Engineers' Handbook, sixth ed., McGraw-Hill, New York, 1984, pp. 3–204;
(d) R.H. Perry, D. Green, Perry's Chemical Engineers' Handbook, sixth ed., McGraw-Hill, New York, 1984, pp. 3–285;
(e) R.H. Perry, D. Green, Perry's Chemical Engineers' Handbook, sixth ed., McGraw-Hill, New York, 1984, pp. 6–22;
(f) R.H. Perry, D. Green, Perry's Chemical Engineers' Handbook, sixth ed., McGraw-Hill, New York, 1984, pp. 2–183 (table 2–200).
[34] (a) R.C. Reid, J.M. Prausnitz, B.E. Poling, The Properties of Gases & Liquids, fourth ed., McGraw-Hill, New York, 1987, p. 441 (Tab. 9–8);
(b) R.C. Reid, J.M. Prausnitz, B.E. Poling, The Properties of Gases & Liquids, fourth ed., McGraw-Hill, New York, 1987, p. 54 (Tab. 3–9);
(c) R.C. Reid, J.M. Prausnitz, B.E. Poling, The Properties of Gases & Liquids, fourth ed., McGraw-Hill, New York, 1987, p. 52;
(d) R.C. Reid, J.M. Prausnitz, B.E. Poling, The Properties of Gases & Liquids, fourth ed., McGraw-Hill, New York, 1987, pp. 602–603;
(e) R.C. Reid, J.M. Prausnitz, B.E. Poling, The Properties of Gases & Liquids, fourth ed., McGraw-Hill, New York, 1987, pp. 598–602;
(f) R.C. Reid, J.M. Prausnitz, B.E. Poling, The Properties of Gases & Liquids, fourth ed., McGraw-Hill, New York, 1987, p. 612.
[35] Data sheets for carbon paper TGP-H-060, supplied by Toray Deutschland GmbH.